

Spatio-temporal dynamics of dilute red blood cell suspensions in a microchannel flow at low Reynolds number

Qi Zhou^{a,1}, Joana Fidalgo^{b,1}, Lavinia Calvi^a, Miguel O. Bernabeu^c, Peter R. Hoskins^d, Mónica S. N. Oliveira^{b,*}, Timm Krüger^{a,*}

^a*School of Engineering, Institute for Multiscale Thermo fluids, University of Edinburgh, Edinburgh EH9 3FB, UK*

^b*James Weir Fluids Laboratory, Department of Mechanical and Aerospace Engineering, University of Strathclyde, Glasgow G1 1XJ, UK*

^c*Centre for Medical Informatics, Usher Institute, University of Edinburgh, Edinburgh EH16 4UX, UK*

^d*Centre for Cardiovascular Science, University of Edinburgh, Edinburgh EH16 4SB, UK*

Abstract

Microfluidic technologies are commonly used for the manipulation of red blood cell (RBC) suspensions and analyses of flow-mediated biomechanics. To maximise the usability of microfluidic devices, understanding the dynamics of the suspensions processed within is crucial. We report novel aspects of the spatio-temporal dynamics of an RBC suspension flowing through a typical microchannel at low Reynolds number. Through experiments with dilute RBC suspensions, we find an off-centre two-peak (OCTP) profile of cells resembling the well-known “tubular pinch effect” which would arise from inertial effects. However, given the negligible inertia under our experimental condition, an alternative explanation is needed for this OCTP profile contrary to the centralised distribution commonly reported for low-inertia flows. Our massively-parallel simulations of RBC flow in real-size microfluidic dimensions using the immersed-boundary-lattice-Boltzmann method (IB-LBM) confirm the experimental findings and elucidate the underlying mechanism for the counterintuitive RBC pattern. By analysing the RBC migration and cell-free layer (CFL) development within a high-aspect-ratio channel, we show that such a distribution is co-determined by the spatial decay of hydrodynamic lift and the global deficiency of cell dispersion in dilute suspensions. We find a CFL development length greater than 46 and 28 hydraulic diameters in the experiment and simulation, respectively, exceeding typical lengths of microfluidic designs. Our work highlights the key role of transient cell distribution in dilute suspensions, which may negatively affect the reliability of experimental results if not taken into account.

Keywords: red blood cells, dilute suspensions, microfluidics, hydrodynamic lift, cell-free layer

1. Introduction

Red blood cells (RBCs) occupy around 45% of the blood volume and play a crucial role in maintaining the normal function of tissues and organs in humans and animals. They transport oxygen and carbon dioxide, regulate blood viscosity, and affect the circulation of nutrients

*Corresponding author e-mail: monica.oliveira@strath.ac.uk or timm.krueger@ed.ac.uk

¹These authors contribute equally to this work.

and immune cells. Pioneered by Chien and Skalak in the 1960s–1980s [1, 2, 3], there has been extensive research carried out theoretically, experimentally and numerically to elucidate the behaviour of single RBC and characterise the dynamics of RBC suspensions (see recent reviews [4, 5, 6, 7, 8]). However, despite major progress, a rigorous and quantitative connection between microscale RBC dynamics and macroscale haemorheology is still lacking [9].

Up to date, various factors affecting blood microrheology have been determined by theoretical/numerical models of RBCs or biomimetic vesicles, including (but not limited to): (i) viscosity contrast (between inner and outer fluids) [10], deformability [11], orientation [12] and initial position [13] of the cell; (ii) shear component (distinct in linear/quadratic flows) [14], suspending viscosity [15], flowline curvature [16] and wall confinement [17] of the flow; (iii) two-body or multi-body hydrodynamic interactions between cells [18]. Most studies focus on the individual dynamics/pairwise interaction of cells or the characteristic signatures of the overall suspension system, e.g., effective viscosity and normal stress differences.

Much less attention has been paid to the collective behaviour of cells, e.g., their spatio-temporal organisation or local microstructures, at a realistic length scale in three-dimensional space. Common reasons for avoiding such studies include their complexity of analytical modelling or prohibitiveness of computational cost. In fact, the RBC behaviour at sub-suspension level plays a key role in bridging the RBC dynamics and haemorheology. A mechanistic understanding of it would help elucidate the onset and progression of blood disorders affecting the cell deformability/mechanical properties (such as malaria, diabetes and sickle cell anaemia), and potentially inspire perspectives for new therapies.

From an experimental perspective, the development in microfluidic technology over the last two decades has provided a powerful tool to explore the otherwise inaccessible behaviour of complex biofluids at the microscale. It is now widely employed for blood flow experiments aimed at various applications [19, 20, 21]. For practical reasons in microfluidics, dilute or semi-dilute RBC suspensions are mainly used, where the clogging of samples is minimal and the measurements of individual cells are quantitatively accurate [22, 23, 24]. Through observation of dilute/semi-dilute RBCs in polydimethylsiloxane (PDMS) microfluidic channels, many intriguing properties of RBC flow at the microscale have been demonstrated, such as uneven cell-plasma partitioning [25], long-range hydrodynamic interaction [26], wall-induced lift of cells in tumbling motion [27], cytoplasmic viscosity-promoted polylobes on cell membrane [28] and diffusion-governed collective spreading of cell suspensions [29].

Recently, Sherwood et al. [30] revealed strongly heterogeneous distribution of cells in a semi-dilute RBC suspension (volume fraction 16%), which presented locally skewed rather than axisymmetric haematocrit (Ht) profiles. With much lower RBC concentration ($\leq 5\%$), Shen et al. [31] found an even more heterogeneous RBC distribution eventually leading to inversion of the classic Zweifach-Fung effect (governing cell partitioning) downstream of bifurcations. These studies imply that the spatial arrangement of RBCs in microchannels can be highly dynamical and alters from one location to another. Such local characteristics, if ignored, may give rise to inaccurate estimation of the haemodynamics in the microfluidic channels, and affect the physiological relevance of the in vitro experiments designed to imitate in vivo systems.

The present work aims to elucidate the spatio-temporal distribution of RBCs in a dilute suspension flowing through a typical microfluidic channel of rectangular cross-section. For a dilute suspension ($Ht \leq 1\%$) of horse RBCs infused into the microchannel, cell density profiles are obtained by a direct cell-counting routine developed *in-house*. As a result, we observe a counterintuitive cell distribution with off-centre two-peak ordering rather than a single peak near the centreline, even in the negligible inertia regime. Immersed-boundary-lattice-Boltzmann simula-

tions performed for an equivalent system confirm the experimental finding and provide insight into the underlying mechanisms.

The paper is organised as follows: the experimental and numerical methods are introduced in Sec. 2. In Sec. 3.1, cell density profiles from experiments and simulations are presented. Sec. 3.2 provides analysis of the observed cross-streamline migration and explores the mechanism behind the density profiles. Sec. 4 compares the present study with existing works and states the key implications of our findings. Sec. 5 concludes the paper.

2. Methods

The employed experimental and numerical methods are outlined in Secs. 2.1 and 2.2, respectively. Further information is provided in the Supplemental Information (SI).

2.1. Microfluidic experiments

2.1.1. Sample preparation and characterisation

RBC suspensions in Dextran40 were prepared using horse blood (see Fig. B1, SI for Photomicrography of the RBC suspension) provided by TCS Biosciences, in anticoagulant EDTA (1.5 mg/mL). The procedures for sample processing are described in Fig. B2 and Sec. B.1 of the SI. The steady shear rheology of Dextran 40 was determined by a rotational rheometer (DHR2, TA Instruments, with minimum resolvable torque 0.1 nNm) using a cone-plate geometry of 60 mm diameter and angle $\theta = 1^\circ$ (CP60/1), 30 μm truncation gap. The density and shear viscosity values used to calculate dimensionless numbers (e.g., Reynolds number and Capillary number) for experiments are 1.07 g/mL and 5.0 mPa s, respectively.

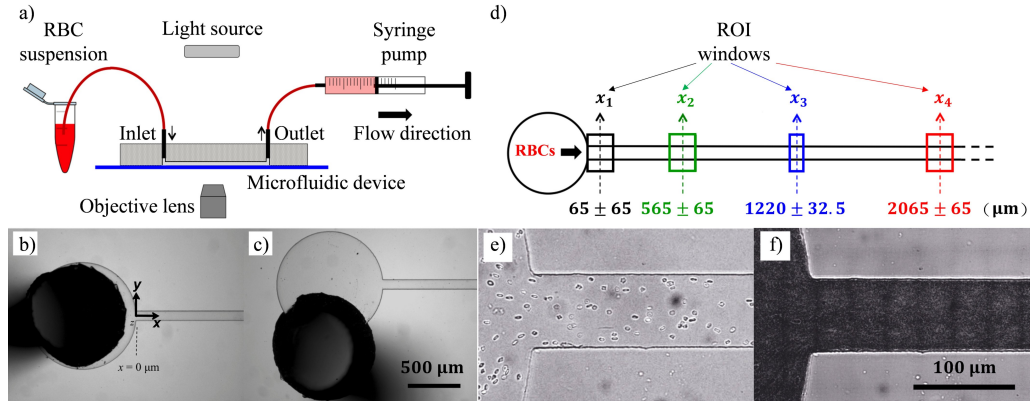


Figure 1: (a) Schematic representation of the experimental setup. (b–c) Inlet configuration of the microfluidic device, showing optical images of the flow entry region where the inlet port is (b) aligned and (c) misaligned relative to the channel centreline. In (b), the coordinate axes are shown. (b–c) share the same scale bar of 500 μm . (d) Schematic showing designated regions of interest (ROIs) for the measurement of probability density distribution (PDD) of RBCs in the suspension. (e) An individual frame of RBCs flowing in the microchannel and (f) a composite image combining 300 frames of the same region, obtained using the Z-projection method based on minimum intensity. In (e–f), $Q = 0.2 \mu\text{L}/\text{min}$, and they share the same scale bar of 100 μm .

2.1.2. Experimental setup and data acquisition

The microfluidic devices were manufactured by soft-lithography using an SU8 mould produced by photo-lithography (microLIQUID). The microfluidic channels were made in PDMS (polydimethylsiloxane, Sylgard 184, Dow Corning) and bonded to a glass slide substrate using oxygen plasma (Zepto, Diener). The channels exhibit a rectangular cross-section ($W \times H = 87 \times 31 \mu\text{m}^2$), with the width and depth dimensions determined by optical microscopy.

Fig. 1a shows a schematic of the experimental setup, where the sample is infused into the inlet of the microdevice using the withdraw function of the syringe pump located at the outlet. With this proposed system, the sample-containing Eppendorf can be gently stirred at regular time intervals to minimise cell sedimentation, which typically limits the duration of experiments. To test the effect of inlet conditions, inlet ports are manually punched onto the PDMS, so that the tubing connection can be either aligned (Fig. 1b) or misaligned (Fig. 1c) with the centreline of the microdevice. The results here presented are for the aligned case, unless otherwise stated.

The experimental setup used an inverted microscope (Olympus IX71) for flow visualisation and a syringe pump (Nemesys, Cetoni) for fluid control. The microfluidic device was illuminated using a halogen lamp. Videos were acquired by a sensitive monochrome CCD camera (Olympus, XM10) using a 10 \times magnification objective with numerical aperture of 0.25 to guarantee that the depth of field and image depth are large enough to observe cell trajectories across the entire channel height (Fig. 1e and Sec. B.2, SI). An algorithm was developed *in-house* based on ImageJ software to detect and count the cells automatically (Fig. B3 and Fig. B4 in Sec. B.2, SI). The RBC probability density distribution (PDD) along the width direction of a given region of interest (ROI, see Fig. 1d) is then calculated using a minimum of 300 frames, containing more than 8,000 cells (Fig. B5 and Fig. B6 in Sec. B.3, SI). The cell-free layer (CFL) is determined as half the difference between the overall channel width and the RBC-core width, using composite images (Fig. 1f) generated via the Z-projection method. The detailed procedure is described Fig. B7 and Sec. B.4 of the SI.

2.2. Computational modelling

2.2.1. Flow solver

The immersed-boundary-lattice-Boltzmann method (IB-LBM [32]) is employed to model blood flow as a suspension of deformable RBCs. The fluid flow governed by the Navier-Stokes equations is solved by the lattice-Boltzmann method with standard D3Q19 lattice [33], BGK collision operator [34] and Guo's forcing scheme [35]. The RBCs are modelled as Lagrangian membranes using a finite element approach (see Sec. 2.2.2). The fluid flow and RBC membrane are coupled through the immersed-boundary method [36], which tackles the interpolation of velocities and the spreading of forces. The model is implemented in the parallel lattice-Boltzmann flow simulator *HemeLB* [37] (open source at <http://ccs.chem.ucl.ac.uk/hemelb>) by incorporating a new module for discrete deformable cells. Details about the model configuration (Fig. C1), simulation setup (Fig. C2) and numerical analysis can be found in Sec. C.1, Sec. C.2 and Sec. C.3 of the SI, respectively. See Table 1 for the key simulation parameters.

2.2.2. RBC model

Each RBC is modelled as a closed finite-element membrane with 720 triangular facets (meshing resolution matching the lattice size Δx for numerical stability and accuracy [38]), with its unstressed shape assumed as a biconcave discoid. The RBC membrane is elastic, with its mechanical properties controlled by five moduli which govern different energy contributions. They

Table 1: Key simulation parameters. The symbol “~” represents simulation units.

Parameter	Symbol	Value
<i>channel geometry</i>		
width	W	96 μm
depth	H	30 μm
length	L	1320 μm
hydraulic diameter	D_h	45.7 μm
entry region diameter	D_{entry}	180 or 96 μm
<i>RBC model</i>		
cell radius	r_{rbc}	4 μm
viscosity contrast	λ	1.0
feeding haematocrit	H_F	1%
local haematocrit	H_t	variable
<i>simulation setup</i>		
particle Reynolds number	Re_p	0.03
capillary number	Ca	0.6
LB relaxation parameter	τ_{BGK}	1.0
voxel size	Δx	0.6667 μm
time step	Δt	$7.41 \times 10^{-8} s$
shear modulus	$\bar{\kappa}_s$	5.00×10^{-4}
bending modulus	$\bar{\kappa}_b$	4.50×10^{-5}
reduced bending modulus	$\bar{\kappa}_b \Delta x^2 / (\bar{\kappa}_s r_{\text{rbc}}^2)$	1/400

are strain modulus κ_s , bending modulus κ_b , dilation modulus κ_a , surface modulus κ_s and volume modulus κ_v . For more details of the RBC model, please refer to [32].

The RBC behaviour in flow is determined by two non-dimensional numbers: the particle Reynolds number Re_p and the capillary number Ca . Re_p represents the ratio of particle inertia to fluid viscous force and is defined based on the channel Reynolds number Re_c :

$$Re_p = Re_c \left(\frac{2r_{\text{rbc}}}{D_h} \right)^2, \quad Re_c = \frac{\rho_{\text{ex}} \bar{u} D_h}{\eta_{\text{ex}}} \quad (1)$$

where r_{rbc} is the RBC radius and D_h is the hydraulic diameter of the rectangular channel; \bar{u} is the cross-sectional mean velocity of the unperturbed flow; ρ_{ex} and η_{ex} are the density and dynamic viscosity of the suspending fluid, respectively.

Ca represents the shear-induced deformation of the RBC membrane and is defined based on the shear elasticity of the RBC membrane:

$$Ca = \tau \dot{\gamma}_c, \quad \tau = \frac{\eta_{\text{ex}} r_{\text{rbc}}}{\kappa_s}, \quad \dot{\gamma}_c = \frac{8\bar{u}}{D_h} \quad (2)$$

where τ is a characteristic time scale for the RBC membrane to relax to its equilibrium shape from a transient state and $\dot{\gamma}_c$ is the characteristic shear rate (wall shear rate in equivalent Poiseuille flow). Both Ca and the viscosity contrast λ (between RBC interior and the suspending fluid) are kept the same for experiments and simulations to ensure comparability (see values in Table 1).

2.2.3. Haematocrit calculation

After the RBCs are fully perfused inside the channel and the number of cells becomes stable, snapshots from multiple time steps of the simulation are extracted and superimposed to calculate the time-averaged haematocrit profile at a given ROI. For the dilute suspension with $H_F = 1\%$, 100 time steps (with 2.22 ms between each) are used to ensure sufficient cells in the sampling pool. Next, various ROIs alongside the channel length are selected to count the cells, starting at a position 150 μm away from the entrance of the main channel. In total, 10 target positions between 150 μm and 1050 μm are chosen, with a 100 μm increment. At each target position, we consider cells contained in a $W \times H \times \Delta L$ sampling box. All cells within this box are counted based on their centre of mass and allocated into N_{bin} subdivisions either along the widthwise (W) direction or the depthwise (H) direction. The local haematocrits $Ht_{(i)}$ in each subdivision are then calculated as

$$Ht_{(i)} = \frac{n_{\text{rbc}(i)} Vol_{\text{rbc}}}{Vol_{\text{bin}}}, \quad Vol_{\text{bin}} = \frac{Vol_{\text{box}}}{N_{\text{bin}}}, \quad (i = 1, 2, \dots, N_{\text{bin}}) \quad (3)$$

where $n_{\text{rbc}(i)}$ is the number of cells detected in a given subdivision, $Vol_{\text{rbc}} = 100 \text{ fL}$ is the standard volume of an RBC, Vol_{bin} is the volume of each subdivision, $Vol_{\text{box}} = W \times H \times \Delta L$ ($\Delta L = 50 \mu\text{m}$) is the volume of the sampling box, and $N_{\text{bin}} = 10$ is the number of subdivisions in Vol_{box} .

3. Results

The experimental and simulation results on the RBC distribution in the channel are shown in Sec. 3.1. Additional data of RBC dynamics and the mechanisms leading to the observed RBC distribution is provided in Sec. 3.2.

3.1. Counterintuitive RBC distribution

The main results of the study are reported here, focusing on the dynamical distribution of RBCs in a dilute suspension. Experimentally, by continuously feeding RBCs at fixed haematocrit ($H_F \leq 1\%$) into the microfluidic device, the transverse motion of cells can be evaluated by monitoring the probability density distribution (PDD) of RBCs at sequential locations along the channel length direction. This process is also replicated numerically to corroborate the experimental observations and provide further insights into the 3D motion of cells in a microchannel of rectangular cross-section.

3.1.1. Experiments

Under negligible inertia ($Re_p < 2 \cdot 10^{-4}$), we observe an evident increase of cell concentration in a region close to each wall, manifested by the augmentation of two off-centre peaks in the PDD profile depicting RBC fractions across the channel (Fig. 2a, $Ca = 0.6$). Locations of the two peaks are approximately symmetric about the channel centreline and keep moving inwards until a certain distance about 0.2~0.25 times the half channel width $W/2$ to the wall is reached (i.e., $y/(0.5W) = 0.75 \sim 0.8$). Beyond this distance, the inward migration of cells ceases (compare $x = 1220, 2065 \mu\text{m}$); this eventually causes an off-centre two-peak (OCTP) ordering in the density profile. Contrarily, in the central region, the cell concentration remains nearly unchanged. By comparing the PDD profiles along the channel length, a cell population originally close to each wall is found to cross streamlines and progressively shift inwards (see $x = 65, 565, 1220 \mu\text{m}$).

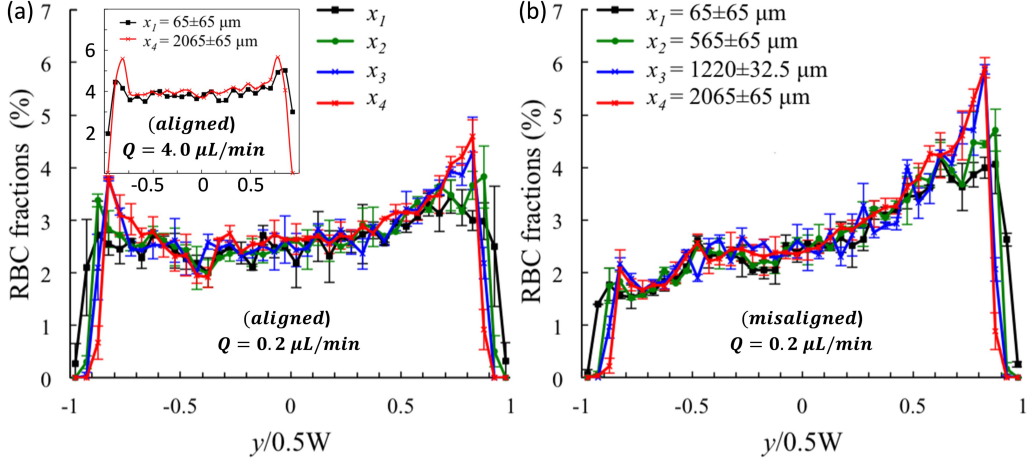


Figure 2: (Experiment) (a–b) Probability density distribution (PDD, see Sec. B.3) of RBCs at $x = 65, 565, 1220, 2065 \mu\text{m}$ away from the entrance, under a volume flow rate of $Q = 0.2 \mu\text{L/min}$. The inlet ports are (a) aligned and (b) misaligned relative to the channel centreline, respectively. The inset of (a) shows the RBC PDD profiles at $x = 65, 2065 \mu\text{m}$ under a volume flow rate of $Q = 4.0 \mu\text{L/min}$ for the aligned configuration.

For an initial cell distribution with significant left-right asymmetry induced by misaligned flow inlet (Fig. 1d), the same inward motion of cells near the wall occurs (Fig. 2b).

The observed quasi-steady OCTP distribution of RBCs does not agree with the commonly reported cell distribution (or haematocrit profile) in microscale channels, which typically exhibits a core of cells near the channel centre accompanied by a cell-depleted layer near the channel wall [39, 40]. To rule out the possibility that such an OCTP distribution is exclusive to the volume flow rate $Q = 0.2 \mu\text{L/min}$ ($Ca = 0.6$), Q is also varied up to $4.0 \mu\text{L/min}$ ($Ca = 12.1$) for the aligned configuration (inset of Fig. 2a). Clearly, the volume flow rate does impact the initial PDD profile at $x = 65 \mu\text{m}$: a low Q (e.g., $Q = 0.2 \mu\text{L/min}$) yields a virtually flat density profile, whereas a high Q (e.g., $Q = 4.0 \mu\text{L/min}$) gives rise to appreciable density peaks near the walls. Despite the dependence of initial RBC distribution on Q (presumably within a range where the cell deformation is sensitive to Ca), qualitatively similar evolution (up to $x = 2065 \mu\text{m}$) of the PDD profile is identified for all cases, featuring the development/enhancement of density peaks at two symmetric locations near the lateral channel walls.

3.1.2. Simulations

To understand the peculiar cell distribution observed in experiments, numerical simulations for a 1% RBC suspension flowing at low Reynolds number ($Re_p = 0.03$) are performed in a long straight microchannel of similar aspect ratio ($W/H = 3.2$). In simulations, we have access to the three-dimensional distribution of RBCs in the channel and can therefore investigate the cell distribution across both directions (Fig. 3a). While results from the width direction (W , top view) can be compared with experimental data, results from the depth direction (H , side view, unobservable from our experimental setup) provide additional insight into the RBC dynamics.

From the calculated histogram of local haematocrits (indicating the Ht profile) at a position near the entrance ($x = 150 \mu\text{m} \approx 3.3D_h$), distinct initial states of the suspension can be found in the width and depth directions upon the entry of RBCs into the rectangular channel. While

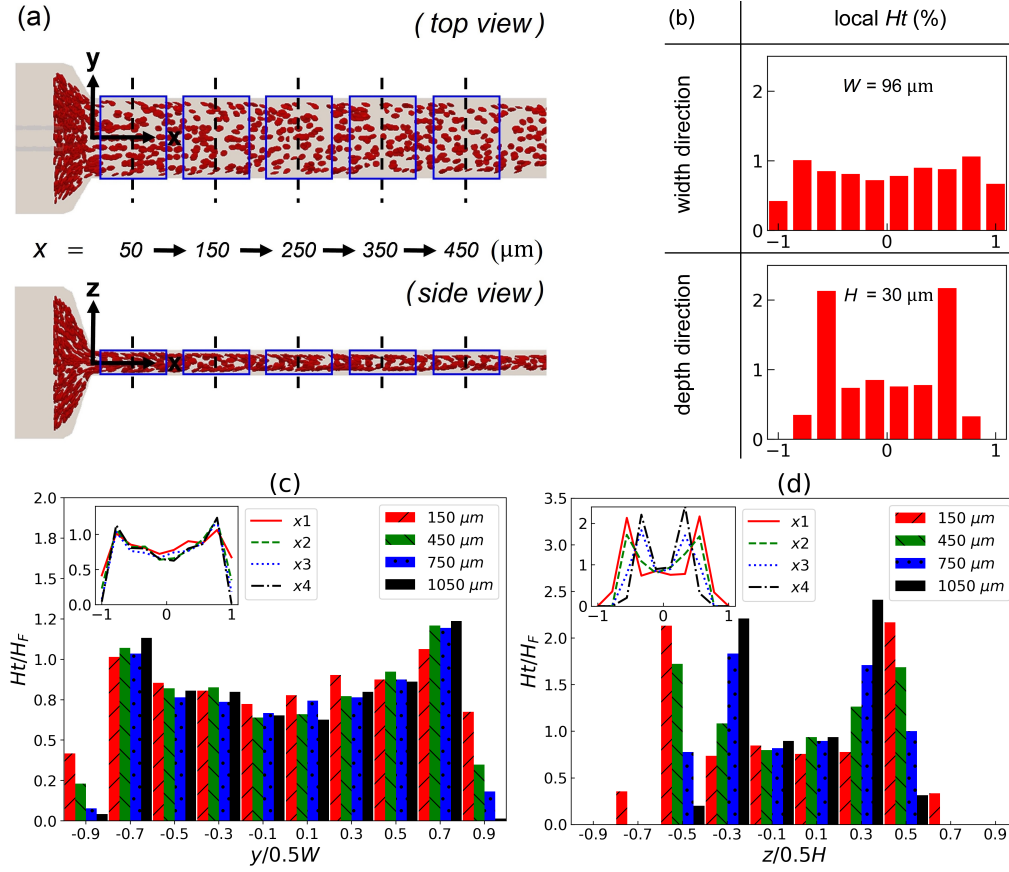


Figure 3: (a) Example of haematocrit (Ht) analysis showing cells superimposed from 5 time steps of the simulation. To calculate the Ht profiles, sequential sampling boxes (blue) measuring $50 \mu\text{m}$ long each are set at target locations (ROIs) along the channel. Cells within each blue box are then counted and allocated into 10 bins across the channel width and depth directions, respectively. The position of each cell is determined based on its centre of mass. (b) (Simulation) Histogram of local Ht measured at $x = 150 \mu\text{m}$ away from the entrance in the width and depth directions, respectively. (c–d) (Simulation) Evolution of the cross-sectional Ht profile alongside the channel in (c) the width direction, and (d) the depth direction, wherein the four colors red, green, blue, black indicate a distance of $x = 150, 450, 750, 1050 \mu\text{m}$ away from the entrance, respectively. All Ht values in (c–d) are normalised by the feeding haematocrit H_F , which equals 1%. The insets within (c–d) show line plots corresponding to the Ht histograms.

the widthwise distribution of cells presents a more or less centralised pattern, the depthwise distribution features two primary density peaks (Fig. 3b). Subsequent Ht profiles monitored at downstream locations ($x = 450, 750, 1050 \mu\text{m}$) bear a general resemblance to the corresponding initial distribution at $x = 150 \mu\text{m}$, indicating the suspension’s persisting memory of the initial state even after a development length $> 20D_h$ (Fig. 3c–d). Specifically, in the W direction, the Ht profiles gradually develops into a two-peak profile with the near-wall cells progressively shifting inwards (Fig. 3c). Conversely, cell densities in the central area only change in a minor way, despite the continuous enrichment of concentration within the neighbouring peaks. This overall trend is in line with our experimental findings of the PDD profile as described in Sec. 3.1.1. Note how the “pseudo-equilibrium” position of the peaks agrees with that found in experiments, being

about 0.3 times of half channel width away from the wall (i.e., $y/(0.5W) = 0.7$).

In the H direction (Fig. 3d), a distinct pattern for the haematocrit profile is the evolution of a five-layered ordering, featuring a cell-depletion layer next to each wall, two cell-enrichment layers neighbouring the centre, and one cell-depression layer right at the centre. Far downstream from the entrance ($x = 1050 \mu\text{m}$), the heterogeneity of cell concentration across the depthwise direction becomes highly pronounced, presenting an arguable equilibrium position for the primary density peaks located at about 0.7 times the half channel depth away from the wall (i.e., $z/(0.5H) = 0.3$). Overall, a substantial inward march of cells towards the channel centreline can be observed, with marked shifts of both density peaks.

3.2. Flow properties and RBC dynamics

To reveal the underlying physics behind the intriguing OCTP distribution of RBCs presented in Sec. 3.1, we investigate several key aspects of the problem, including the origin of transverse cell migration, the effect of channel geometry, the distribution of cell velocity, the formation of the cell-depletion layer and the variation of tube haematocrit. The two main questions we aim to address are: 1) How do the two density peaks in the PDD profile come into being? 2) Why do the peaks keep building up instead of being dispersed?

3.2.1. Mechanism for cell migration

Given its small Reynolds number, our RBC flow practically falls into the low-inertia regime, where viscous effects dominate. For deformable objects in viscous flow, the phenomenon of their lateral drift away from the wall is well-documented, dating back to the 1830s when Poiseuille first observed a plasma layer (or cell-free layer, CFL) in frog arterioles and venules [41]. The origin of such motion of RBCs was later determined to be the non-inertial hydrodynamic lift arising from unbalanced pressure forces on the cell. This lift can drive cells in microscale vessels/channels to cross streamlines and migrate towards the central area, ultimately leading to the formation of a two-phase flow featuring a cell core and a fluid periphery [39, 40].

Following the discovery by Goldsmith and Mason [42], the lateral migration of deformed particles in non-inertial flows has been confirmed by other experimental studies [43, 44, 45, 46] and numerous modelling reports [47, 48, 49, 50, 51, 52, 53, 54, 55]. In principle, there are three mechanisms for the cross-streamline motion of RBCs in low-Reynolds-number shear flows: 1) wall-repulsion-induced lift force on RBCs, 2) shear-gradient-induced asymmetric deformation of RBCs, and 3) hydrodynamic diffusion (or shear-induced diffusion) between RBCs due to cell-cell interactions. Depending on the flow properties (e.g., velocity profile, shear distribution and wall confinement) and cell conditions (e.g., position, shape and rigidity), the direction and strength of RBC motion under the combined effect of the above mechanisms can be difficult to determine.

3.2.2. Geometric effect and shear anisotropy

In our problem, where a laminar flow is pressure-driven in a rectangular microchannel of high aspect ratio ($W/H = 3.2$), the flow field is complex because distinct velocity profiles co-exist in the channel cross-section: a typical parabola characteristic of Poiseuille flow in the depth (H) direction and a blunted profile featuring plug-like flow in the width (W) direction [56]. Additionally, the existence of entrance effects further increases the complexity of the problem. These two aspects contribute to a plethora of scenarios for the velocity profile curvature (reflecting the shear-rate gradient), which on the one hand constitutes a mechanism for cell migration itself (by introducing symmetry-breaking deformation [50]) and on the other hand impacts the wall-induced lift (being a function of the particle shape [57]). We show the evolution of unperturbed

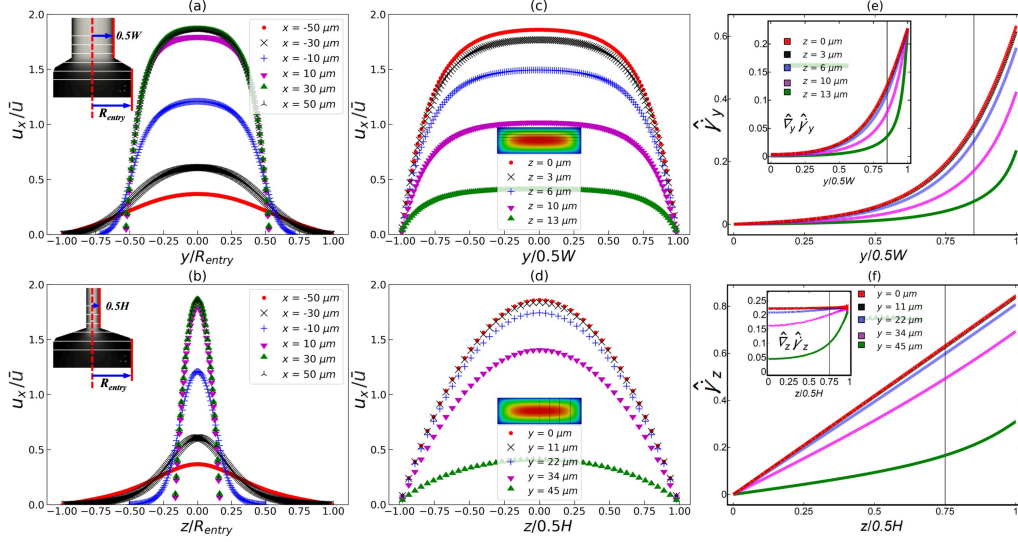


Figure 4: 3D flow in the rectangular channel. (a–b) (Simulation) Transient mid-plane velocity profiles near the entrance at positions labelled by white solid lines in the channel sketch. (c–d) (Simulation) Steady velocity profiles at $x = 50 \mu\text{m}$. z and y values in the legends represent positions relative to the mid-plane in each direction, with $z = 0$ and $y = 0$ denoting the widthwise and depthwise mid-planes, respectively. (e–f) (Analytical) Shear rates (main frame) and shear-rate gradients (inset) calculated from asymptotic solutions in [56]. The colors represent z or y values as in (c–d). The black vertical lines in (e–f) indicate the center of the outmost layer of cells at $x = 50 \mu\text{m}$ detected in the RBC simulation along the (e) y -direction and (f) z -direction, respectively (see Fig. 5).

mid-plane velocity profiles (in the absence of cells) near the entrance across both directions, where rich behaviour of the velocity profile can be found as the fluid accelerates through the contracted transition between the entry region and the channel itself (Fig. 4a–b). This geometry-induced velocity alteration potentially underpins the distinct initial distribution of RBCs between the W and H directions of the channel observed in Fig. 3b.

Fig. 4a–b reveal that the flow becomes fully-developed between $x = 30\text{--}50 \mu\text{m}$ in our simulations. Fig. 4c–d show the converged velocity profiles for different z - and y -planes at $x = 50 \mu\text{m}$, respectively. Using the asymptotic solution of this microfluidic flow [56], we further calculate and plot the shear-rate profiles and shear-rate-gradient profiles. The cross-sectional pattern of shear rates (normalised by the time scale τ as in Eq. 2) turns out more intricate than often assumed (Fig. 4e–f), even in the narrow dimension (H) where linearity is commonly assumed for such a high aspect ratio ($W/H > 3$) [46]. At close distances to the wall (e.g., $y = 45 \mu\text{m}$ in Fig. 4d), the H -direction velocity profile deviates significantly from a parabolic one (Fig. 4f), resulting in non-linear decrease of shear rate on approaching the channel centreline and varying shear gradients (inset of Fig. 4f). In the W direction where blunted velocity profiles prevail (Fig. 4c), the shear gradients vary both at close and large distances to the wall (inset of Fig. 4e), leaving the hydrodynamic lift even more unpredictable by the classic theory derived on the basis of ideal shear flows [57] (to be further discussed in Sec. 4.1.1).

3.2.3. Decay of lift velocity

The presence of RBCs at $H_F = 1\%$ and below does not disturb the apparent velocity profiles significantly from their unperturbed states (Fig. C3 in Sec. C.4, SI), we can therefore analyse the

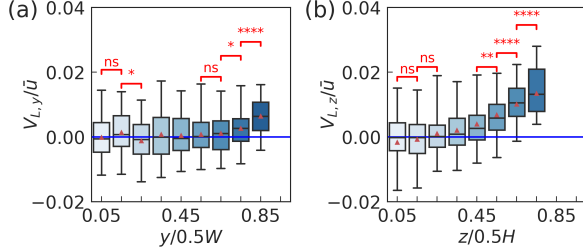


Figure 5: (Simulation) Statistical lift velocities of RBCs within $x = (50 \pm 8) \mu\text{m}$, characterising the RBC migration along the (a) y -direction (widthwise) and (b) z -direction (depthwise), respectively. For statistical analysis in both (a) and (b), the channel is fictitiously folded along the channel centreline and then divided into 10 bins, followed by the assignment of cells according to the position of their center of mass. A positive lift velocity here indicates an inward motion of RBCs towards the channel centreline.

*Statistics note: the black solid line and the red triangle inside each box represent the median and the mean lift velocity within each bin, respectively. The horizontal hats (red) above the boxes show results of independent two-sample T-tests between neighbouring cell groups, where $*P < 0.05$ is considered as statistical significance; $**P < 0.01$, $***P < 0.0001$.*

transverse motion of RBCs with respect to the channel wall based on the unperturbed flow. From the properties of the unperturbed flow elaborated in Sec. 3.2.2, such motion of RBCs are likely to be affected by both the solid wall and the fluid shear gradients. At low Reynolds number, this motion can be conveniently decomposed into two orthogonal directions, hereby the W and H directions, on assuming negligible inertia and invoking the Stokes equations. Fig. 5a–b show the statistical lift velocities V_l of the cells (relative to the unperturbed flow mean velocity \bar{u}) in 10 subdivisions of a cross-section, divided either widthwise (W) or depthwise (H). Compared with the depthwise lift, the widthwise lift is found to decay much faster as the cell-wall distance increases. While $V_{l,z}$ vanishes at 0.75 times of $H/2$ away from the wall ($z/(0.5H) = 0.25$), $V_{l,y}$ already becomes negligible at 0.35 times of $W/2$ away from the wall ($y/(0.5W) = 0.65$). The contrast of lift decay between the two directions can be explained by trends of the shear rate profile and the shear gradient profile in the cross-section (Fig. 4e–f). As the cells migrate towards the channel centreline, the local shear rate diminishes to zero, with much faster drop in W direction than in H . Meanwhile, the local shear gradient also quickly diminishes to zero in W direction, whereas that in H direction decreases in a much milder way. Consequently, both contributions of the wall-induced lift and shear-gradient-induce lift in the W direction are weakened more quickly.

The distribution of lift velocities in both the width and depth directions coincides with the overall evolution of the Ht profiles presented in Fig. 3c–d: while a “pseudo-equilibrium” position close to the wall exists for the widthwise migration (beyond which the lateral motion of cells ceases), the depthwise cell migration is more substantial and results in a “pseudo-equilibrium” position much closer to the channel centre. Therefore, a correlation between the decaying lift of cells and their spatial distribution in the cross-sectional direction can be inferred.

3.2.4. Growth of cell-free layer

We now move on to investigate how the transverse motion of RBCs contributes to the spatial development of CFL along the channel axis. Shown in Fig. 6a is the growth of CFL thickness over $46D_h$ in experiments (recording the averaged CFL from the two lateral walls). The data manifests an evident power-law behaviour with a best-fit exponent of 0.39 ($R^2 = 0.93$). The simulation CFLs over $28D_h$ (recording separate CFLs for individual lateral/vertical walls) present similar trends, also showing a power-law increase (inset of Fig. 6a). However, further scrutiny of the simulation data reveals a slight discrepancy in the growth rate (Fig. 6b). Compared to the

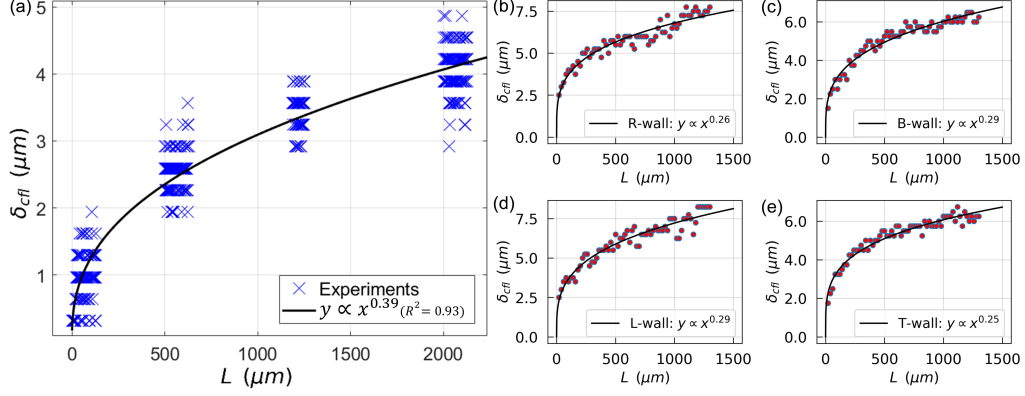


Figure 6: (a) (Experiment) CFL measured in the width direction of the channel (averaged between opposite walls) under $Q = 0.2 \mu\text{L}/\text{min}$ ($Ca = 0.6$). (b–e) (Simulation) Power-law fitting for numerical CFLs from an equivalent simulation ($Ca = 0.6$) developing along each wall of the channel (right/bottom/left/top walls). The R-square values are 0.91, 0.94, 0.91, 0.95 for the R-/B-/L-/T-walls, respectively.

experimental value of 0.39, the power-law exponents we found in the simulation are smaller. In the width direction, the exponents are 0.26 and 0.29 for the right and left walls, respectively; in the depth direction, they are 0.29 and 0.25 for the bottom and top walls, respectively. Further analysis and quantification of this discrepancy between experimental and simulation CFL will be discussed in Sec. 4.1.2, with support from a scaling law we derived for the current problem.

Despite the difference between the growth rates of experimental and simulation CFL, a neutral finding is that no critical saturation of the CFL increase can be identified throughout the investigated range. This means that the development of CFL in a typical microfluidic channel (rectangular cross-section) for a dilute suspension can take much longer than earlier estimates provided for microvessels or cylindrical tubes [58, 59, 60, 61]. In particular, Katanov et al. [59] reported a universal length $L_c \leq 25D$ (independent of flow rate and haematocrit) for full CFL development in vessels between $D = 10\sim 100 \mu\text{m}$, whereas we find $L_c > 28D_h$ in simulation (only serving as a lower-bound estimate because we have limited our flow domain to such a length for tractable computational cost) and $L_c > 46D_h$ in experiment (hydraulic diameter of the channel $D_h \approx 45.7 \mu\text{m}$). Based on our numerical findings of the “pseudo-equilibrium” positions for the widthwise cell migration (until 0.3 times of half channel width from wall) and depthwise cell migration (until 0.7 times of half channel depth from wall), the CFL thickness in the simulation may continue to grow until reaching $10\sim 14 \mu\text{m}$, which are considerably larger than the values of $6\sim 8 \mu\text{m}$ we have monitored within $L_c \leq 28D_h$ (Fig. 6b).

3.2.5. Reduction of tube haematocrit

The long-range development of CFL will inevitably affect the local rheological properties of the suspension. As shown in Table 2, the tube haematocrit H_t measured from either of our simulated geometries (see CTRAC-L (large contraction, all simulation data and plots presented elsewhere in the paper are from this geometry) and CTRAC-S (small contraction) defined in Sec. C.1 of the SI) drops continuously along the channel axis compared to the feeding haematocrit H_F , even after $1050 \mu\text{m}$ ($\approx 23D_h$) away from the entrance. This reduced volume fraction of blood flow in microchannels versus the discharge haematocrit ($H_D \approx H_F$) is known as the

Table 2: (Simulation) Variation of tube haematocrits along the channel axis.

Inlet type	H_F	Ht -150 μm	Ht -450 μm	Ht -750 μm	Ht -1050 μm	Ht -1150 μm
CTRAC-L	1%	0.810%	0.749%	0.703%	0.696%	0.685%
CTRAC-S	1%	0.705%	0.661%	0.659%	0.622%	0.619%

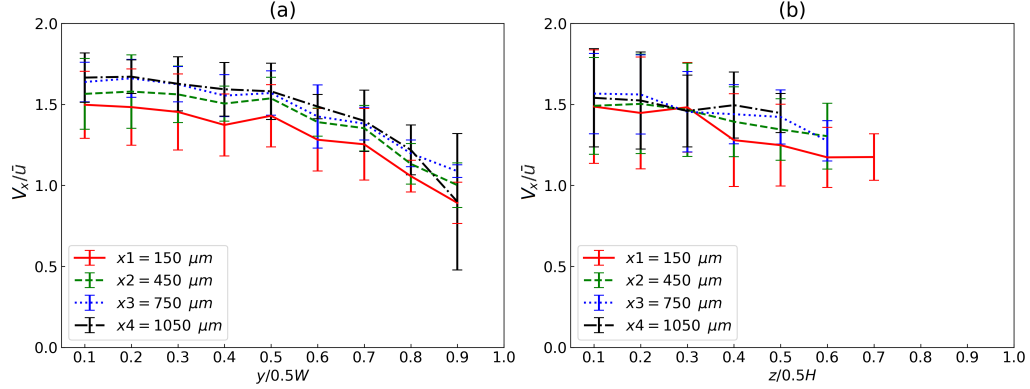


Figure 7: (Simulation) Axial (streamwise) velocity of RBCs V_x in the channel (normalised by mean velocity of the unperturbed flow \bar{u}) at $x = 150, 450, 750, 1050 \mu m$ away from the entrance. (a) and (b) show the width and depth directions of the channel, respectively. For statistical analysis in both (a) and (b), the channel is fictitiously folded along the channel centreline and then divided into 10 bins, followed by the assignment of cells according to the position of their center of mass. Each error bar here shows the mean and standard deviation of the streamwise velocity.

Fåhræus effect, where $Ht/H_D = \bar{U}_B/\bar{V}_x < 1$ (\bar{U}_B and \bar{V}_x are average velocities of the overall blood flow and the cells, respectively) [62, 63]. It stems from the cross-streamline motion of RBCs towards the high-velocity region around channel centreline, which empowers the cells within the channel to travel faster on average than the ambient fluid in the streamwise direction. Owing to the fairly long CFL development length ($> 28D_h$ in simulation), the cross-sectional distribution of RBC fluxes (Fig. C4 in Sec. C.5, SI) and consequently the average ratio of cell-to-fluid velocities (Fig. 7) continues to change till the very end of the channel, leaving consistent measurement of tube haematocrits within the microchannel difficult.

4. Discussion

In the following we will discuss and compare our findings in Sec. 3 with existing studies and interpretations, and elaborate on their implications for microfluidic studies of dilute blood flow.

4.1. Comparison with existing studies

4.1.1. Hydrodynamic lift

Empirical laws. The mechanism of hydrodynamic lift for tank-treading particles in shear flows has been analysed theoretically by Olla and Seifert in the 1990s [64, 65]. A simplified scaling law $V_l \sim \dot{\gamma}/h^2$ was derived for the lift velocity V_l under constant shear, as a function of the shear rate $\dot{\gamma}$ and cell-wall distance h [57]. This quadratic scaling has been widely employed in the literature as an approximation to estimate the lateral migration of particles in various flow conditions. However, recent studies show that in pressure-driven channel flows where non-constant shear (or

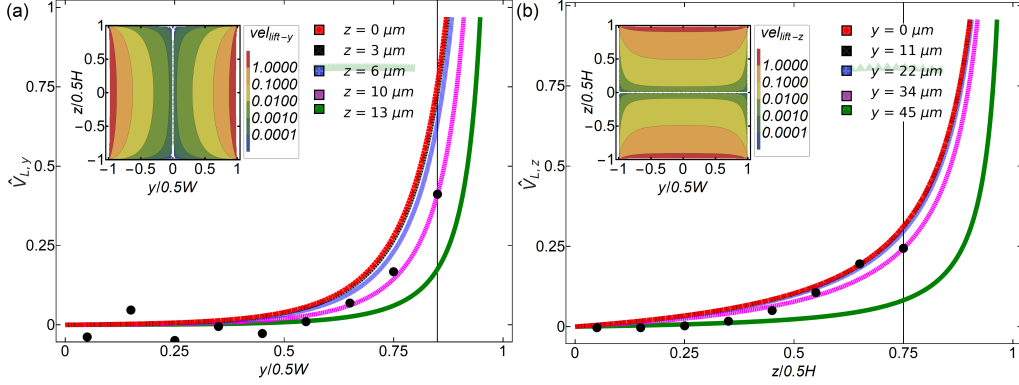


Figure 8: Theoretical prediction (line curves in the main frame and contour plots in the inset) of RBC lift velocities given by $V_l \sim \dot{\gamma}/h$ across (a) the width direction, and (b) the depth direction of the channel, respectively. z and y values in the legends represent positions relative to the mid-plane in each direction (same to Fig. 4c–d), with $z = 0$ and $y = 0$ denoting the widthwise and depthwise mid-planes, respectively. For comparison with the theoretical prediction, median values of the numerical lift velocities extracted from Fig. 5a–b are rescaled and fitted onto the line curves as black dots. The black vertical lines in (a–b) indicate the center of the outmost layer of cells at $x = 50 \mu\text{m}$ detected in the RBC simulation along the (a) y -direction and (b) z -direction, respectively (see Fig. 5).

non-zero shear gradient) exists, e.g., Poiseuille flow, the curvature of the velocity profile modifies the scaling law in a non-trivial way and would significantly slow down the spatial decay of the lift velocity [50, 66, 55, 67]. Indeed, through systematic measurement of the lateral migration of various vesicles in bounded planar Poiseuille flow under different confinement degrees, Couplier et al. revealed that the scaling $V_l \sim \dot{\gamma}/h^2$ would fail to predict the trajectory of the vesicle, while a markedly different empirical law $V_l \sim \dot{\gamma}/h$ held [46]. Losserand et al. confirmed the scaling $V_l \sim \dot{\gamma}/h$ using RBC experiments and further refined the empirical law [68].

Simulation. To examine whether the lateral migration of RBCs in our simulation obeys the lift scaling that Couplier et al. [46] and Losserand et al. [68] proposed for Poiseuille flow, we adopt theoretical shear rates from the asymptotic solution of pressure-driven flow in rectangular channel [56] and calculate the lift velocities applying $V_l \sim \dot{\gamma}/h$ (abandoning all prefactors for generality). Further with weighted normalisation, we obtain the dimensionless theoretical lifts ($\hat{V}_{l,y}$ and $\hat{V}_{l,z}$) for both W and H directions (Fig. 8a–b). For comparison with the theoretical prediction, numerical medians of our numerical lift velocities are extracted from Fig. 5a–b. After rescaling and overlapping them onto the theoretical curves, we observe satisfactory data agreement across the H direction but only partial agreement in the W direction for the near-wall region only. Approaching the central region in the W direction, the theoretical prediction breaks down. This is actually expected since the velocity profile there is abruptly blunted and significantly deviates from a parabolic shape. We have also examined against our simulation data the theoretical prediction given by $V_l \sim \dot{\gamma}/h^2$, which would overestimate the spatial decay of the lift in general and failed to yield an agreement with the simulation data (results not shown here).

4.1.2. Cell-free layer

Background. CFL characterisation is an active research field owing to the prominent role of CFL in regulating blood viscosity and local haemodynamics. Limited by the complexity of in vivo imaging and measurement [69], glass capillaries and PDMS microchannels have been widely

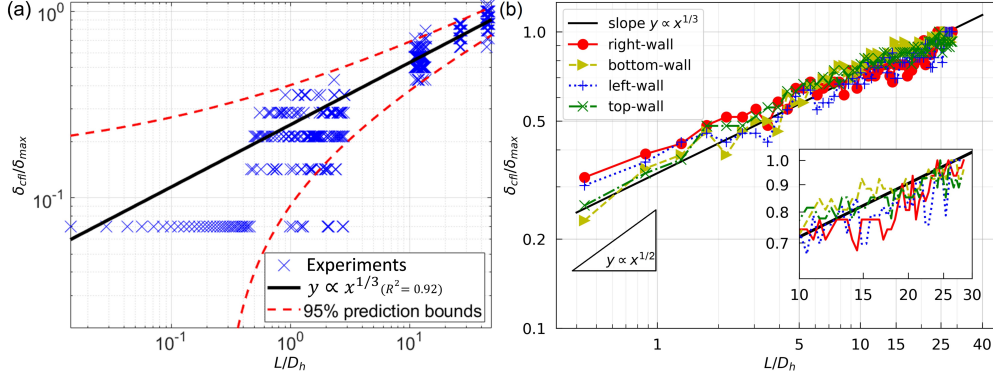


Figure 9: Regression analysis of the CFL development, presenting log-log plots of the (a) experimental and (b) numerical CFLs as in Fig. 6. All CFL values δ_{cfl} are normalised by the maximum CFL thickness δ_{max} detected within the full range of channel length, and the development lengths L are normalised by the channel hydraulic diameter D_h . The inset of (b) shows a zoom-in view of the numerical CFL trends within $L = 10 \sim 28D_h$.

used to mimic the micro-circulatory environment for experimental observation of CFLs in vitro under different rheological conditions [70]. Meanwhile, versatile computational tools are developed and plenty of in silico studies on CFL emerge in the literature [40]. However, despite the large number of in vitro/in silico studies, most of them assumed a steady CFL for a given channel segment and hence failed to capture the highly heterogeneous and spatio-temporal nature of realistic CFLs as in the microcirculation [71, 72]; albeit some authors were aware of this problem and proposed a nominal CFL development length denoting the product of the development time and the mean flow velocity [15, 59]. It is only recently that exact analyses of the spatio-temporal heterogeneity of CFL were presented [73, 60, 74], detailing the spatial development/recovery of the CFL alongside microchannels in the presence of upstream disturbances.

Scaling analysis. In the present problem, having confirmed the spatial variation of lift velocity $V_1 \sim \dot{\gamma}/h$ (rather than $V_1 \sim \dot{\gamma}/h^2$) against the cell-wall distance h for individual RBCs (Sec 4.1.1), estimation can be made for the longitudinal development of δ_{cfl} in a dilute suspension using an analytical approach (see Sec. A of the SI for further details). Our derivation shows that considering $a = 1$ in Eq. (A.1) (corresponding to $V_1 \sim \dot{\gamma}/h$) yields a power-law scaling for the CFL as expressed in Eq. (A.11): $\delta_{\text{cfl}} \sim \ell^\beta$, $\beta = 1/3$, where ℓ is the axial distance along the channel. The exponent of $1/3$ here is surprising as it coincides with the power-law scaling for vesicle/RBC motion in simple shear flow with constant shear rate (see Eq. 3 in [45]). Note that because $\delta_{\text{cfl}} \sim \ell^{1/3}$ is derived on the basis of a parabolic velocity profile under the assumption of planar Poiseuille flow (constant shear-rate gradient), whereas the flow patterns in a real microchannel are far more complex (Sec 3.2.3), its accuracy for the prediction of spatial CFL development remains to be verified by our numerical data and experimental measurements.

Simulation and experiment. The power-law growth $\delta_{\text{cfl}} \sim \ell^{1/3}$ predicted by the scaling analysis assuming ideal Poiseuille flow (Sec. A, SI) turns out to lie between our experimental and numerical trends, the best-fitted power-law exponents for which are 0.39 and 0.25~0.29, respectively (Fig. 6). Through regression analyses of the experimental and numerical data in log-log scales, both data sets are found to compare well with $\delta_{\text{cfl}} \sim \ell^{1/3}$ (Fig. 9a–b). Furthermore, for the numerical data, the instantaneous slopes in the log-log graph are found to be nearly independent of ℓ at

the early stage of CFL development, presenting a roughly steady increase of $1/3$ (Fig. 9b). This implies the predominant role of a single mechanism for the transverse motion of cells, which is sensibly the hydrodynamic lift as our scaling analysis suggests. Moving downstream of the channel, a continual increase of the CFL thickness is observed upon approaching $\ell = 28D_h$, but with slower growth indicated by decreasing slopes (noticeably smaller than the original $1/3$, see the inset of Fig. 9b). This deceleration in CFL growth is expected down to the fact that the lift forces are weakened as the cells migrate further away from the wall and enter the low-shear region with blunted velocity profiles, where the lateral motion of cells will slow down.

In simulations of much denser RBC suspensions ($Ht = 15\% \sim 45\%$) in cylindrical tubes [59], a similar power-law behaviour was reported for the steep increase of CFL thickness at an initial development stage (before a second time scale induced by relaxation of the RBC core came into play). However, the power-law exponents reflected by the authors under a range of shear rates were in general smaller than the value of $1/3$. The deviation from $1/3$ was caused by the cell-cell interactions existing in a dense suspension, which obstructed the initial migration of RBCs and led to slower CFL growth than what could happen in a dilute suspension. Arguably, the authors reasoned for the ideal growth factor of $1/3$ by invoking the lift force scaling $F_l \sim V_l \sim 1/h^2$ (where $\dot{\gamma}$ is a constant and does not affect the scaling) derived from simple shear flows [48, 52]. Albeit such reasoning does explain the qualitative trend of their CFL growth, the simple shear flow approximation itself for quadratic flows in a microchannel (where $\dot{\gamma}$ varies) is questionable, which may fail to capture important features of the RBC distribution in the presence of shear rate gradients as recent theories of particle migration at low Reynolds number demonstrate [75, 76].

4.2. Implications and limitations

What we have covered so far not only elucidates the “aberrant” RBC distribution observed in our experiment and simulation contradicting earlier findings, but also has wider implications for experimentalists working on dilute suspensions in high-aspect-ratio microfluidic devices. In brief, microfluidic designs need to be longer if their purpose is to investigate the microscopic behaviour of a dilute suspension *after* completed lateral migration. Experimentally, it is notoriously difficult to accurately control the inlet distribution of a cell/particle suspension under various *entrance effects*. Therefore, local observations are frequently reported based on the assumption that the suspension organisation is free of transient effects at the chosen region of interest (ROI) as long as the ROI is adequately far away from the entrance. However, the required length as revealed by our study turns out more demanding than commonly believed [59, 58, 60, 61]. Some key messages are:

- For experiments of a dilute RBC suspension in *high-aspect-ratio* microfluidic channels, the hydrodynamic lift of RBCs are substantially suppressed due to the existence of low-shear-rate and low-shear-gradient zones in the centre. Consequently, the full development of a CFL in these channels may require a much longer development length ($L_c > 28D_h$ in simulations and $L_c > 46D_h$ in experiments) than what is normally expected for cylindrical tubes ($L_c \leq 25D$ according to [59]). Furthermore, the relevance of *in vivo* measurements of cellular behaviour using such high-aspect-ratio microchannels to the realistic microcirculatory blood flow needs reappraisal. After all, the vessels in the microcirculation are more likely to have circular cross-sections and considerably different velocity profiles, which the radial distribution of RBCs heavily relies on.
- When determining the organisation of a dilute suspension (e.g., haematocrit profile) in a typical microchannel of rectangular cross-section, local measurements may be misleading

if the channel is short or only moderately long. This is because heterogeneities emerging in the suspension (e.g., density peaks) will persist and hinder the formation of an equilibrium cell distribution due to the lack of RBC dispersion under *weak cell-cell interactions*. In particular, if certain upstream disturbance exists (e.g., geometric constriction or expansion), history effects need to be considered when recording local rheological properties such as the tube haematocrit. Comparing the cases CTRAC-S and CTRAC-L in Table 2, with channel geometry, unperturbed flow rate and feeding haematocrit all being the same, yet the tube haematocrits measured at sequential locations constantly differ by more than 6% (relative change). The reason is simply their differently configured flow inlets, causing unequal degrees of disturbance to the initial distribution of cells within the suspension.

- Phenomena violating empirical laws may occur downstream of bifurcations if the upstream RBC suspension is at an intermediate stage of development and has special cell distribution, e.g., the OCTP profile observed in our study. Recently, counterintuitive inversion of haematocrit partition against the classic Zweifach-Fung effect in a bifurcating microfluidic channel was reported by Shen et al., arising from the formation of consecutive layers of high and low RBC haematocrits in the parent branch [31]. The juxtaposed configuration of RBCs discovered by that study is in line with the five-layered ordering of cells we find in the depth direction of our RBC flow (Fig. 3). Therefore, the phenomenon Shen et al. captured might also have been a consequence of insufficient channel length for the suspension to be fully developed in the parent branch.

Some limitations of the present study are: 1) While the numerical model simulates human RBCs, horse RBCs are used in experiments due to laboratory restrictions. This may have caused a certain degree of discrepancy between the simulation and experiments. The influence on results of the suspension behaviour should be limited to quantitative instead of qualitative differences, given the comparable size and biomechanical properties of both RBC types. 2) The effect of inlet configuration on suspension organisation has not been systematically characterised in a quantitative manner, which can potentially provide more specific guidance for experimentalists to improve their microfluidic designs by reducing transient effects. We aim at addressing this issue in a future study, involving geometric factors such as constrictions, expansions and bifurcations. 3) The experimental data is insufficient for analysis of instantaneous growth rates of the CFL thickness as has been performed for the simulation. More measurements from a denser arrangement of ROIs, though quite challenging, should be made in future experiments in order to enable point-wise local comparison with simulations. 4) To make the full-range (channel length > 1 mm) simulation tractable, we have largely reduced the parameter space and refrained from a comprehensive investigation of multiple flow scenarios (e.g., various volume flow rates with either higher or lower channel aspect ratios) and cell conditions (e.g., pathologically stiffened or sickle-shaped RBCs). A parametric study integrating all these effects will lead to enhanced understanding of the intricate behaviour of dilute suspensions processed in microfluidic devices.

5. Conclusion

We performed both microfluidic experiments and numerical simulation of dilute blood suspensions in a low-Reynolds-number channel flow ($Re_p \ll 1$). Surprisingly, an off-centre two-peak (OCTP) ordering of RBCs was found, which is reminiscent of the “tubular pinch effect”

typical of the radial distribution of particles in inertial microfluidics [77, 78]. However, the transverse motion of cells in our case has an entirely different origin: the non-inertial hydrodynamic lift of deformable particles [42].

Back to the two primary questions we set out to address (see the opening paragraph of Sec. 3.2): how do the two density peaks in the PDD profile come into being and why do the peaks keep building up instead of being dispersed? The reason behind the persistence of significant density peaks is the deficiency of hydrodynamic interactions among cells in the dilute limit, where shear-induced diffusion remains weak and falls short to smooth out density heterogeneities brought by the lateral migration of cells. Consequently, the evolution of the density profiles is predominantly determined by the decay of hydrodynamic lift within the suspension, which exhibits distinct patterns in the width and depth directions of a high-aspect-ratio microchannel and contributes to a counterintuitive (OCTP) profile of cells in the larger dimension. Additionally, depending on the inflow configuration, the initial distribution of cells upon their entry into the channel varies substantially, which brings extra complexity to the restoration of a converged density profile and the development of an equilibrium cell free layer.

Our findings highlight the importance of local and transient characteristics at the dilute limit for an RBC-laden flow in microchannels. Experimentalists should therefore be cautious when working with dilute suspensions in microfluidics and make judicious assumptions about suspension properties with the presence of upstream disturbance to the flow, especially when the microscopic behaviour of the suspension is the focus of research.

Acknowledgements. QZ thanks the University of Edinburgh for the award of a Principal’s Career Development Scholarship and an Edinburgh Global Research Scholarship. TK’s and MOB’s contributions have been funded through two Chancellor’s Fellowships at The University of Edinburgh. MOB is supported by grants from EPSRC (EP/R029598/1, EP/R021600/1), Fondation Leducq (17 CVD 03), and the European Union’s Horizon 2020 research and innovation programme under grant agreement No 801423. Supercomputing time on the ARCHER UK National Supercomputing Service (<http://www.archer.ac.uk>) was provided by the “UK Consortium on Mesoscale Engineering Sciences (UKCOMES)” under the EPSRC Grant No. EP/R029598/1.

SUPPLEMENTAL INFORMATION (SI)

A. Scaling analysis

RBC migration. Consider an RBC whose center of mass is initially located at a position (x_0, y_0) in close proximity to the wall ($y = 0$) upon entry into a microchannel of hydraulic radius R_h . To make the asymptotic analysis tractable, we consider a unidirectional flow along the axial direction of the channel with velocity $u_x(y)$, which is a function of the distance to the channel wall. Driven by the flow, the RBC will gradually migrate towards the channel centreline ($y = R_h$) under hydrodynamic lift while travelling along the streamwise direction (i.e., x -direction), for which the motion can be described by a two-component velocity $v(v_x, v_y)$. Note that v is deliberately used here to represent cell velocity while u is reserved for fluid velocity. For leading-order estimation, we assume $v_x := u_x(y)$. Based on the empirical law by Losserand et. al, we propose an expression for the lift velocity of the RBC v_y as

$$v_y = \dot{y} = K\dot{\gamma}(y)y^{-a}, \quad \dot{\gamma}(y) = \frac{\partial u_x(y)}{\partial y}, \quad (\text{A.1})$$

where $\dot{\gamma}$ is the shear rate of the unperturbed flow, and K and a are constants depending on flow conditions and cell properties. For a given period of time, e.g., $t \in [0, t']$, the RBC travels to a new position (x', y') , and the axial distance ℓ can be written as

$$\ell = x' - x_0 = \int_0^{t'} v_x \, dt = \int_{y_0}^{y'} u_x(y) \frac{dt}{dy} dy = \int_{y_0}^{y'} \frac{u_x(y)}{\dot{y}} dy. \quad (\text{A.2})$$

Combining Eqs. (A.1) and (A.2), one finds:

$$\ell = \frac{1}{K} \int_{y_0}^{y'} y^a v_x(y) \left(\frac{\partial u_x(y)}{\partial y} \right)^{-1} dy. \quad (\text{A.3})$$

On assuming Poiseuille flow, the form of u_x is known and v_x may be expressed as

$$v_x = u_x(y) = \hat{u}_x \left(1 - \left(\frac{R_h - y}{R_h} \right)^2 \right), \quad \hat{u}_x = 2\bar{u}, \quad (\text{A.4})$$

where \hat{u}_x and \bar{u} are the maximum and mean flow velocity, respectively. By replacing v_x in Eq. (A.3) with the above, one gets:

$$\ell = \frac{1}{2K} \int_{y_0}^{y'} y^{a+1} \left(2 + \frac{y}{R_h - y} \right) dy. \quad (\text{A.5})$$

Given that lateral migration of the RBC away from the wall happens very slowly, we may further assume that $y \ll R_h$ over the time scale of our investigation. This means $y/(R_h - y)$ is small, which allows us to arrive at a straightforward expression of the axial distance ℓ that can be integrated over the lateral displacement:

$$\ell \approx \frac{1}{K} \int_{y_0}^{y'} y^{a+1} dy = \frac{y^{a+2}}{(a+2)K} \Big|_{y_0}^{y'}. \quad (\text{A.6})$$

After some rearrangement, we may write the equation as

$$y' = \left((a+2)K\ell + y_0^{a+2} \right)^{\frac{1}{a+2}}. \quad (\text{A.7})$$

CFL development. Now let us consider an arbitrary RBC cloud in the microchannel flow setting off from the wall. It is actually the outermost cells of the cloud that determine the CFL thickness δ_{cfl} , representing the distance between the RBC membrane and the wall. At high Ca numbers (e.g., $Ca = 0.6$), the RBCs are highly deformable and significantly elongated along the flow, and δ_{cfl} can be approximated by y , namely the distance of the RBC's centre of mass to the wall:

$$\delta_{\text{cfl}}(0) \approx y_0, \quad \delta_{\text{cfl}}(t') \approx y'. \quad (\text{A.8})$$

Combining Eqs. (A.7) and (A.8), we arrive at an expression describing the growth of δ_{cfl} along the channel axis at sequential positions of ℓ :

$$\delta_{\text{cfl}}(t') = \left((a+2)K\ell + \delta_{\text{cfl}}(0)^{a+2} \right)^{\frac{1}{a+2}}. \quad (\text{A.9})$$

Ideally, if the outermost cells are directly in contact with the wall, $\delta_{\text{cfl}}(0) = 0$. This simplification results in a power-law scaling between δ_{cfl} and ℓ , with an exponent of β :

$$\delta_{\text{cfl}} \sim \ell^\beta, \quad \beta = \frac{1}{a+2}. \quad (\text{A.10})$$

Specifically, for $a = 1$, corresponding to $V_1 \sim \dot{\gamma}/h$, the exponent becomes $1/3$ and the below scaling holds:

$$\delta_{\text{cfl}} \sim \ell^{1/3}. \quad (\text{A.11})$$

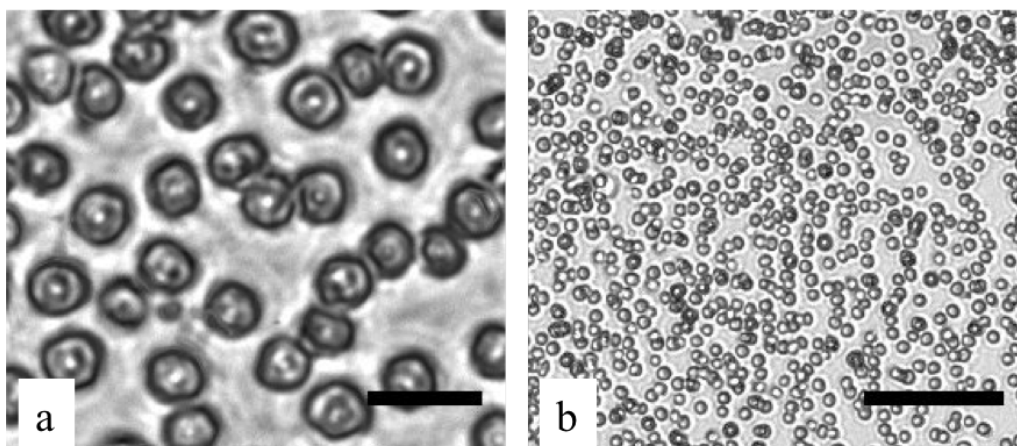


Figure B1: Photomicrography of the horse RBC suspension in PS (NaCl 0.9% w/v) at different magnifications. (a) 40x, scale bar 10 μm ; (b) 10x, scale bar 50 μm .

B. Experiments

B.1. Preparation of RBC suspensions

The RBC suspensions were prepared using horse blood (Fig. B1) instead of human blood due to laboratory restrictions. The blood sample was provided by TCS Biosciences (UK), in anticoagulant ethylenediaminetetraacetic acid (EDTA) 1.5 mg/mL, and stored at 4 °C until further use. Sample processing and disposal were performed following the Ethics Committee for Animal Experimentation at University of Strathclyde. Since the blood was provided from different animals in distinct periods, the packed cell volume (PCV) or haematocrit could range from 30 to 50%, according to the blood provider. This variability is overcome by producing cell suspensions from the cell sediment after washing and centrifugation. The haematocrit (Ht), defined by the cell volume fraction, is controlled to be $Ht \leq 1\%$.

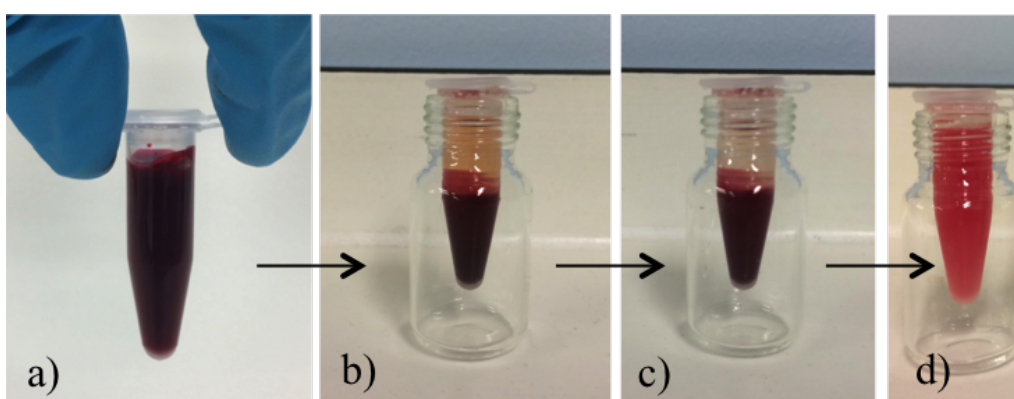


Figure B2: Steps involved in the preparation of RBC suspensions. (a) Eppendorf with whole blood; (b) separation (by centrifugation) of the supernatant plasma and buffy coat from the RBCs sediment; (c) transparent supernatant after RBC washing and centrifugation with PS; (d) RBC suspension in Dx40 solution ($Ht \leq 1\%$).

Fig. B2 presents the steps involved in sample processing. First, an Eppendorf with 1.5 mL of whole blood (WB) was centrifuged at 6000 rpm for 1 min (miniFUGE), after which the supernatant containing the yellow plasma and buffy coat (mainly white blood cells and platelets) was discarded. Second, the RBCs were washed twice with physiological saline PS (NaCl 0.9% w/v), with the transparent supernatant discarded. Third, the final sample was prepared by suspending the desired volume of RBC in Dextran40 solution (Dx40 $M_w = 40000$ g/mol, 0.1 g/mL in isotonic medium). This suspending medium will avoid the phenomenon of cell sedimentation during experiments, which is a common problem for suspensions prepared in PS or in original blood plasma.

B.2. Data acquisition and image analysis

An inverted microscope (Olympus, IX71) was used to observe the device with bright field, employing a small magnification objective (10x/0.25 NA) in order to inspect cells across the entire channel depth and throughout a relatively large section of the channel length. For each flow condition tested, the system was allowed to stabilize for a few minutes before image acquisition by a sensitive monochrome CCD camera (Olympus, XM10) at a frame rate of 15 Hz. The exposure time was set to 100 μ s allowing well-defined images of the cell boundaries. Videos of at least 300 frames each, corresponding to approximately 20 seconds of experiment, were acquired for four regions of interest (ROI). All the images were obtained at the channel centreplane ($z = 0$).

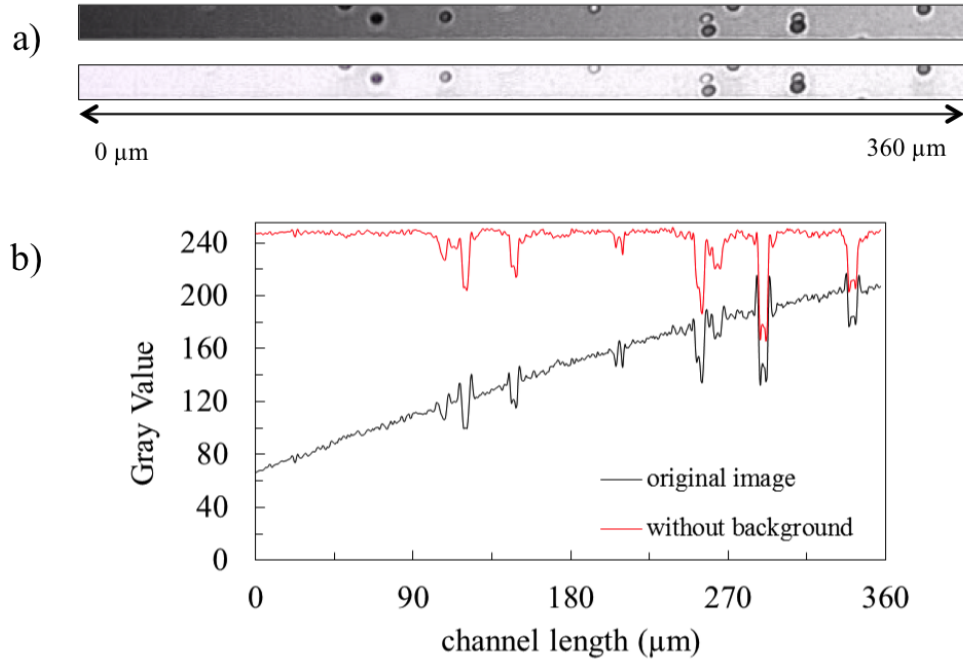


Figure B3: Background correction using Rolling Ball Radius function in ImageJ. (a) Image sections before and after background subtraction; (b) Corresponding intensity profiles to the image sections in (a).

All ROIs have a length of $130\text{ }\mu\text{m}$, except the one corresponding to position $x_2 = 1220 \pm 32.5\text{ }\mu\text{m}$, which is of half that length, i.e., $65\text{ }\mu\text{m}$.

The images acquired need post-processing for image enhancement and cell detection. For this purpose, we applied an automatic cell counting routine developed *in-house* on ImageJ software.

B.2.1. Background correction

The bright field images obtained from experiments usually present an unbalanced intensity distribution, in particular close to the channel inlets and outlets, where the fittings are connected to the device. To enhance the images, they were first corrected by subtracting the background. For this purpose, the Rolling ball radius filter was used, applying a radius of 10 pixels, which corresponds to an approximate diameter of a horse RBC ($D_{RBC} \approx 6\text{ }\mu\text{m}$). This procedure allowed obtaining a clear and balanced image without losing information of the RBC (Fig. B3), especially for those cells located far away from the focal plane.

B.2.2. Cell detection

The RBCs in images with corrected background are then detected and counted using an automatic routine developed on ImageJ open software. Fig. B4 describes the intermediate steps for further image enhancement and cell detection, based on the image with corrected background.

First, a binary image (Fig. B4b) is generated from the image with corrected background (Fig. B4a), followed by function Dilate (Fig. B4c) and function Fill holes (Fig. B4d). This procedure allows recovering the cell contour for brighter cells that are located away from the focal plane. Subsequently, function Watershed is applied to generate separation among slightly overlapped cells (Fig. B4e). Then, function Outline allows delimiting each foreground object in the binary image, by generating a one-pixel wide outline (Fig. B4f). Based on this image, function Analyse Particles provides information of each delimited object, following which the Circularity filter is applied to detect objects whose circularity is in the range of $0.5 \sim 1.0$, defined by $4\pi A/P^2$ (where A is the cell area and P the cell perimeter). The output is the image presented in Fig. B4g, providing numbered cells together with a list of values including the center of mass (X_{COM} , Y_{COM}) and perimeter of each cell. A second filter is applied to the perimeter of the automatic detected object, in order to delete the ones presenting even smaller sizes than an undersized cell ($D_{RBC} \approx 4\text{ }\mu\text{m}$).

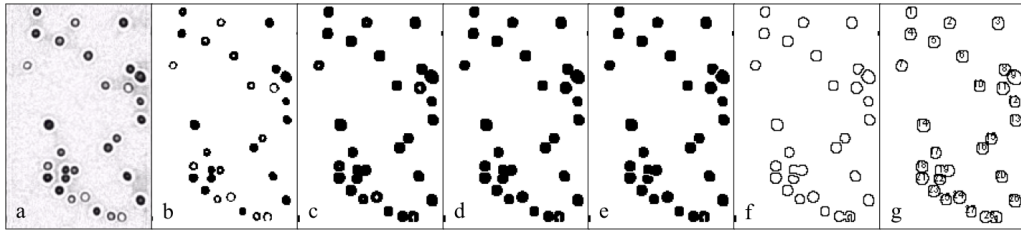


Figure B4: Procedures of detecting cells from the experimental images. (a) Image with corrected background; (b) The corresponding binary image; (c) function Dilate; (d) function Fill Holes; (e) function Watershed; (f) function Outline; (g) detected cells after function Analyse Particles on applying the Circularity filter.

B.3. Probability density distribution (PDD) of RBCs

B.3.1. Calculation of local RBC fractions

Local RBC fractions in experiments are determined using the center of mass information from detected cells within each ROI. We first divide the whole width of the channel into a number of bins (≥ 26) and apply the Frequency function in Excel to count the number of cells that fall into each bin. The RBC fraction for each bin is then calculated as respective cell percentage (%) relative to the total number of cells detected across the whole channel width. Such relative calculation of RBC fractions is to counterbalance the cell counting error arising from the automatic detection method, which does not allow accurate recording of absolute cell numbers because of the interference from cell overlapping in experimental images. By plotting the RBC fractions on the cross-section of the designated ROI, the Probability density distribution (PDD) of RBCs is obtained, which can be regarded as an approximate representation of the haematocrit profile.

B.3.2. Accuracy of the PDD profile

To verify the accuracy of PDD profiles depicting RBC distribution obtained from the automatic counting method, two validation tests were performed. First, we examined the minimum number of frames needed to ensure a converged distribution. For a given ROI, the RBC distribution was determined using four different image stacks, containing 50, 100, 200 and 300 image frames, respectively. The PDD profiles resulting from a relatively small stack, e.g., 50 and 100 frames, were found to present significant noises and differ much from each other (Fig. B5a). In contrast, the distributions obtained from a larger stack, namely 200 and 300 frames, were much smoother and appeared similar to each other (Fig. B5a). Therefore, we conclude that a stack with 300 frames is enough to generate a converged RBC distribution.

Second, we compared the RBC distribution obtained from our automatic counting using a stack of 300 frames with one based on manual counting. The result showed a high-level similarity between the two distributions (Fig. B5b), hence validating the accuracy of our proposed method for the analysis of RBC distribution in experiments using low haematocrit ($Ht \leq 1\%$), where the boundaries of individual cells can be well defined.

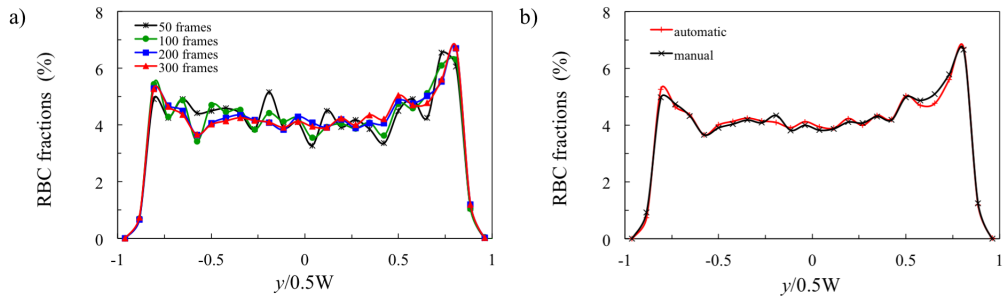


Figure B5: (a) Effect of the number of frames on the RBC distribution calculated by the automatic cell counting method. The PDD profiles are calculated using a stack of 50 frames (black line), 100 frames (green line), 200 frames (blue line) and 300 frames (red line), respectively. (b) PDD profiles (using a stack of 300 images) obtained from automatic cell counting (red line) and manual cell counting (black line), respectively.

B.3.3. Effect of cell overlapping

The effect of cell overlapping is also investigated. In Fig. B4g, it is possible to observe false “agglomerates” (given the RBC concentration and the type of Dextran used in our experiments,

we expect no physical aggregation) caused by the overlapping of cells across the channel depth direction. To study the impact of these “agglomerates” on the calculated RBC distribution, they were identified and excluded in a test case. The resulting RBC distribution was then compared to the original RBC distribution, where the two distributions obtained are found virtually identical (Fig. B6). This suggests that the statistical effect of cell overlapping is negligible on the final cell distribution obtained using our automatic counting method.

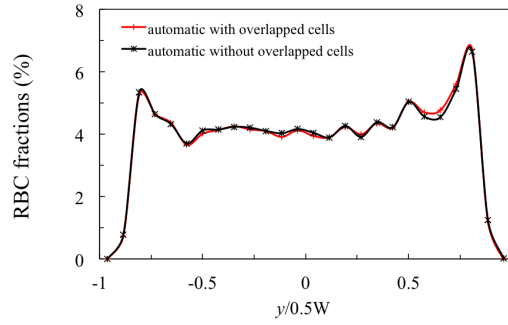


Figure B6: Effect of cell overlapping on the calculated RBC distribution, showing PDD profiles obtained from automatic counting with (red line) and without (black line) overlapped cells in the images, respectively.

B.4. Cell-free layer (CFL)

To measure the CFL at a ROI within the channel, a combined image of 300 frames via minimum intensity Z-projection is generated (Fig. B7a). Using this method, if a cell is passing through the ROI with lower intensity than the background, it will be registered; with a sufficient number of image frames, the layer depleted of cells (CFL) close to the walls can be distinguished. The binary image of such a projection (Fig. B7b) presents a sharp boundary separating the RBC core and the CFL. The average CFL thickness is then defined as half of the averaged difference between the channel width and the RBC core along the ROI.

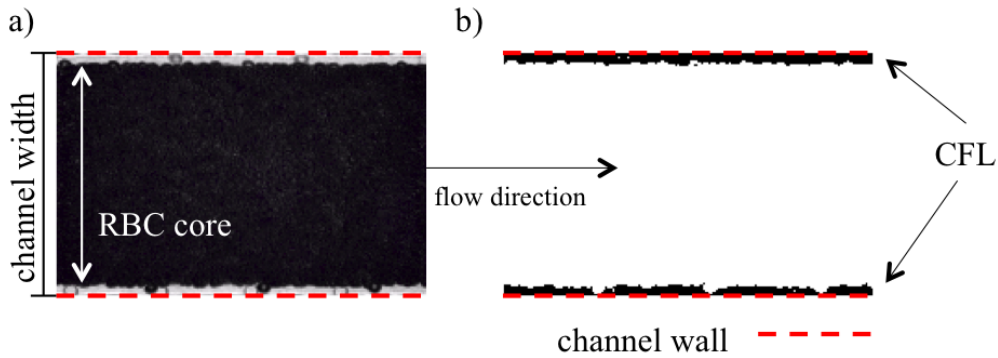


Figure B7: Determination of the CFL thickness. (a) Minimum intensity Z-projection image using a stack of 300 frames. (b) Binary image of the Z-projection for calculation of the CFL thickness.

C. Simulations

C.1. Model configuration

Fig. C1 shows the three-dimensional computational model for simulation of the RBC flow through a rectangular microchannel. Two geometries have been designed in the simulation to account for potential entrance effects that exist in experiments due to inlet configuration, which primarily arise from the inflow contraction between the entry region and the main channel. The main channel part in both geometries is the same, which is $96\ \mu\text{m}$ wide, $30\ \mu\text{m}$ deep and $1.32\ \text{mm}$ long. The only difference is the front-end diameter of the tapered entry region ($100\ \mu\text{m}$ long). The entry region for the first geometry has a front-end diameter of $96\ \mu\text{m}$ (hereafter referred to as CTRAC-S, meaning “smaller (inflow) contraction”), and the one for the second geometry has a front-end diameter of $180\ \mu\text{m}$ (hereafter referred to as CTRAC-L, meaning “larger (in-flow) contraction”). All simulation data and plots presented in this paper are from CTRAC-L, unless otherwise specified). An identical entry region is also added to the channel outlet for removing cells from the simulation. The whole domain measures $1.52\ \text{mm}$ in length, with a total of 26,201,764 lattice voxels (each $\Delta x = 2/3\ \mu\text{m}$). All dimensions of the domain are labelled in Fig. C1, shown from three camera views.

C.2. Simulation setup

To start the simulation, a unidirectional flow is driven from left to right along the x-axis direction (Fig. C2). The flow is controlled by imposing a parabolic velocity profile (assuming Hagen-Poiseuille flow with fixed volume flow rate) at the inlet and a reference pressure at the

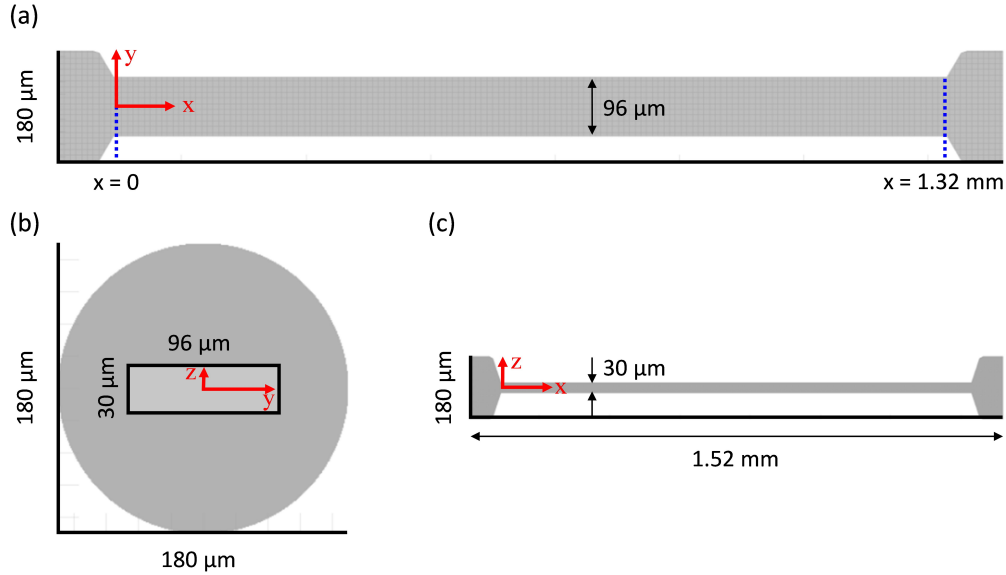


Figure C1: Geometry of the computational model (CTRAC-L, larger contraction). (a) is the top view of the geometry, showing the widthwise span of the channel. In (a), the main channel (rectangular) is marked with two blue dotted lines. (b) shows cross-sectional views of the front-end and rear-end of the tapered entry region, the latter of which coincides with the channel entrance ($x = 0$). (c) is the side view of the geometry, showing the depthwise span of the channel.

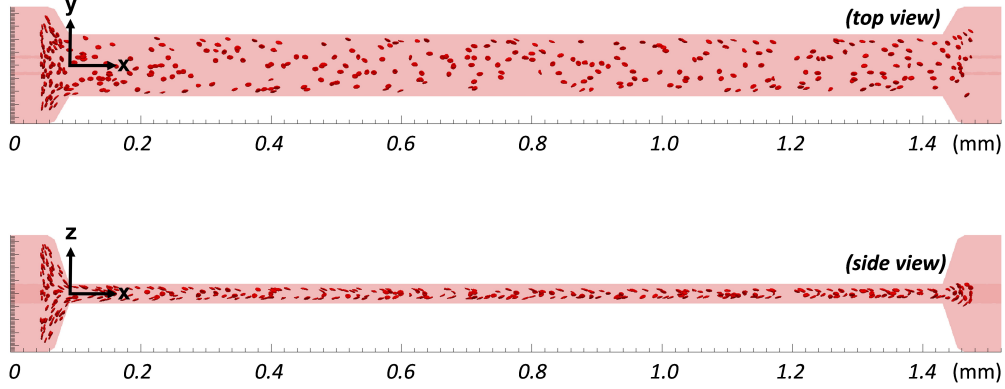


Figure C2: A snapshot of the simulation at $t = 0.37s$, showing distribution of the 1% RBC suspension in the width direction and the depth direction of the microchannel, respectively.

outlet. The no-slip condition on walls is implemented with the Bouzidi-Firdaouss-Lallemand method (BFL [79]). Because it is computationally prohibitive to simulate the realistic experimental condition where the Reynolds number of the flow approaches zero, the fluid flow in our simulation is numerically accelerated to a state where the Reynolds number equals 1. To make the experiments and simulations comparable, we establish the similitude law based on the capillary number Ca . For the target $Ca = 0.6$, we have very deformable RBCs in the channel assuming tank-treading motion, where the cell membrane is fluidized and rolls around the cell interior.

C.3. Numerical analysis

C.3.1. Calculation of RBC velocities

The lateral or axial velocity for an RBC is calculated as the unit displacement of its center of mass along the specific direction over a unit time step in the simulation:

$$V_{l,y} = \Delta L_y / \Delta t, \quad V_{l,z} = \Delta L_z / \Delta t, \quad V_x = \Delta L_x / \Delta t \quad (C.1)$$

Because the trajectories for all RBCs are recorded throughout the simulation, it is straightforward to group the cells into bins according to the location of their center of mass and conduct statistical analysis to estimate the time-average lift velocity (Fig. 5) or streamwise velocity (Fig. 7) of cells at a given position in the microchannel.

C.3.2. Calculation of RBC fluxes

Based on the tube haematocrits $H_{t(i)}$ (subdivided into N_{bin} bins, Eq. 3) at a distance x downstream of the flow inlet, the cross-sectional RBC fluxes $Q_{rbc(i)}$ allocated into the same number of bins can be calculated via the discharge haematocrit $H_{D(i)}$ and blood volume flow rate $Q_{B(i)}$:

$$Q_{rbc(i)} = H_{D(i)} Q_{B(i)}, \quad (i = 1, 2, \dots, N_{bin}) \quad (C.2)$$

$$H_{D(i)} = H_{t(i)} \left(\frac{\bar{V}_{x(i)}}{\bar{U}_{B(i)}} \right), \quad Q_{B(i)} = \bar{U}_{B(i)} A_{bin} \quad (C.3)$$

where $A_{\text{bin}} = W \times H/N_{\text{bin}}$ is the cross-sectional area of each bin, and $\bar{V}_{x(i)}$ and $\bar{U}_{B(i)}$ are the spatial-average RBC velocity and blood flow velocity within each bin, respectively. Combining Eqs. (C.2) and (C.3), we have the following equation to be used for RBC flux calculation:

$$Q_{\text{rbc}(i)} = H t_{(i)} \bar{V}_{x(i)} A_{\text{bin}} \quad (\text{C.4})$$

C.3.3. Calculation of cell-free layer

To characterise the CFL in a rectangular channel with width W and depth H , we consider a cross-section at a distance x downstream of the flow inlet to be divided into four triangles by the diagonals. The heights of the four triangles, each perpendicular to a channel wall, are located at $\theta = 0, \pi/2, \pi, 3\pi/2$, respectively. We define the RBC density $\phi(h, \theta', x, t)$ at a point $p(x, h, \theta')$ of longitudinal coordinate x , height coordinate h and angular coordinate θ' within a given triangle for a certain time instant t as 1 if that point is enclosed by at least one RBC membrane; otherwise, $\phi(h, \theta', x, t) = 0$. The time-mean RBC density within any of the four triangles can then be obtained via integration over (h, θ') and average over t :

$$\bar{\phi}(x, \theta) = \frac{1}{N} \sum_{i=1}^N \int_0^{L_h} \int_{\theta-\Theta/2}^{\theta+\Theta/2} \phi(h, \theta', x, t_i) h \tan |\theta' - \theta| d\theta' dh \quad (\text{C.5})$$

wherein N is the number of time steps extracted from the simulation, L_h is the height of the triangle and Θ is its tip angle centred in the cross-section. For the left and right triangles:

$$L_h = W/2, \quad \Theta = 2 \arctan(H/W) \quad (\text{C.6})$$

and for the top and bottom triangles:

$$L_h = H/2, \quad \Theta = 2 \arctan(W/H) \quad (\text{C.7})$$

If we define the CFL as a thin layer in proximity to a given wall (or the base of a given triangle) which contains only a negligible fraction of RBC density ε , e.g., $\varepsilon = 1e-6$, then the thickness of this layer $\delta(x, \theta)$ can be determined using numerical iterations:

$$\varepsilon = \frac{1}{\bar{\phi}(x, \theta) N} \sum_{i=1}^N \int_{L_h-\delta(x, \theta)}^{L_h} \int_{\theta-\Theta/2}^{\theta+\Theta/2} \phi(h, \theta', x, t_i) h \tan |\theta' - \theta| d\theta' dh \quad (\text{C.8})$$

By calculating $\delta(x, \theta)$ for each θ at consecutive x locations, we can obtain the CFL thickness for each wall along the channel axis direction (Fig. 6).

C.4. Disturbance of RBCs to the plasma flow

The velocity profiles from the RBC-laden flow at Ht 1% (Fig. C3) apparently do not deviate much from the unperturbed flow in the absence of RBCs (Fig. 4). This implies that the sparse distribution of RBCs in the dilute limit only affects the flow velocity to a limited amount and causes local disturbances without modifying the overall velocity profile significantly. Therefore, it is reasonable to analyse the migration of RBCs in the 1% suspension using the unperturbed plasma flow.

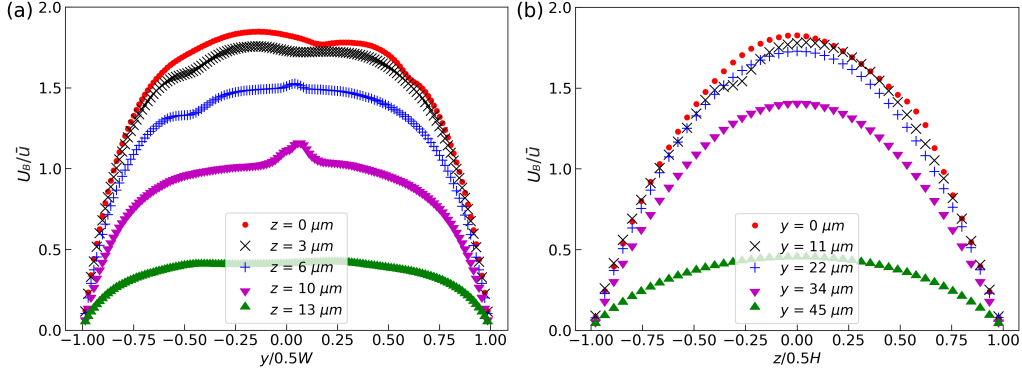


Figure C3: Velocity profiles of the RBC-laden flow at $x = 50 \mu\text{m}$. The z and y values in the legends represent positions relative to the mid-plane in each direction, with $z = 0 \mu\text{m}$ and $y = 0 \mu\text{m}$ being the width and depth mid-planes, respectively. The blood velocities U_B are all normalised by mean velocity of the unperturbed flow \bar{u} .

C.5. Cross-sectional RBC flux distribution

The Ht profile is co-determined by the lateral migration (toward channel centreline) and the streamwise acceleration (along channel axis) of RBCs, the former of which arises from the hydrodynamic lift effect and the latter is associated with the Fåhræus effect. Both effects have an impact the distribution of local haematocrits and can affect the dynamical evolution of the Ht profile. In this sense, the peaks emerging in the Ht profile (Fig. 3) may not be ideal markers of the “pseudo-equilibrium” position for the inward migration of cells. Therefore, to ascertain the “pseudo-equilibrium” positions suggested by Ht peaks, these two effects need to be decoupled. To this end, we calculate the RBC fluxes, the sum of which strictly conserves along the channel axis and examine the cross-sectional distribution of the RBC fluxes. This allows us to exclude the effect of cell acceleration and distinguish the amount of lateral migration of the cells (Fig. C4).

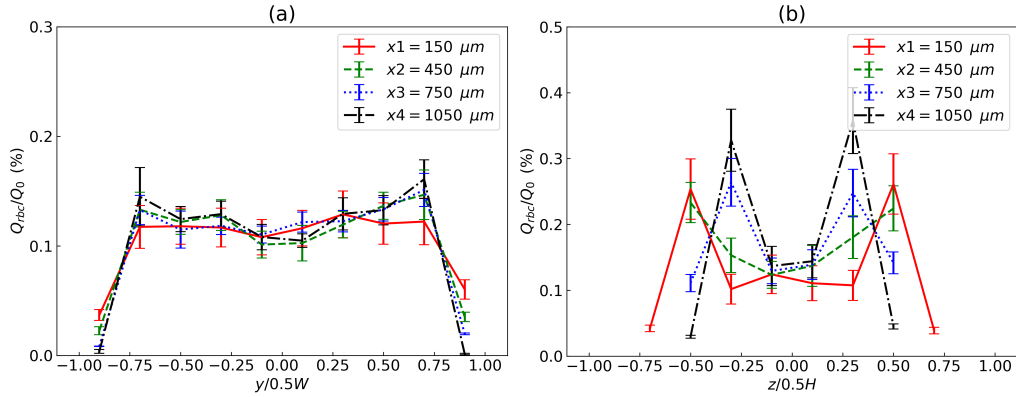


Figure C4: (Simulation) Evolution of the cross-sectional RBC fluxes alongside the channel in (a) the width direction, and (b) the depth direction. The four colors red, green, blue, black indicate a distance of $x = 150, 450, 750, 1050 \mu\text{m}$ away from the entrance, respectively. The RBC fluxes Q_{RBC} are all normalised by the volume flow rate of the unperturbed flow Q_0 , and then converted to percentage (%).

The evolution of RBC-flux distribution turns out qualitatively similar to that of the Ht profiles. It reveals a clear trend of inward RBC migration over time, with near-wall RBC fluxes moving away and subsequently accumulating at a “pseudo-equilibrium” position in both directions of the channel. For the widthwise migration, this equilibrium position is found to be 0.3 times of half channel width away from the wall; for the depthwise migration, it is 0.7 times of half channel away. The inward shift of RBC fluxes is accompanied by the continuous expansion of a zero-flux zone in the vicinity of the wall, which corresponds to the gradually growing CFL.

References

- [1] S. Chien, S. Usami, R. J. Dellenback, M. I. Gregersen, L. B. Nanninga, M. M. Guest, Blood Viscosity: Influence of Erythrocyte Aggregation, *Science* 157 (1967) 829–831.
- [2] S. Chien, R. G. King, R. Skalak, S. Usami, A. L. Copley, Viscoelastic properties of human blood and red cell suspensions, *Biorheology* 12 (1975) 341–346.
- [3] R. Skalak, S. Chien, Rheology of blood cells as soft tissues, *Biorheology* 19 (1982) 453–461.
- [4] P. M. Vlahovska, D. Barthes-Biesel, C. Misbah, Flow dynamics of red blood cells and their biomimetic counterparts, *Comptes Rendus Physique* 14 (2013) 451–458.
- [5] D. Abreu, M. Levant, V. Steinberg, U. Seifert, Fluid vesicles in flow, *Advances in Colloid and Interface Science* 208 (2014) 129–141.
- [6] J. Freund, Numerical Simulation of Flowing Blood Cells, *Annual Review of Fluid Mechanics* 46 (2014) 67–95.
- [7] T. M. Geislinger, T. Franke, Hydrodynamic lift of vesicles and red blood cells in flow — from Fåhræus & Lindqvist to microfluidic cell sorting, *Advances in Colloid and Interface Science* 208 (2014) 161–176.
- [8] A. Yazdani, X. Li, G. E. Karniadakis, Dynamic and rheological properties of soft biological cell suspensions, *Rheologica Acta* 55 (2016) 433–449.
- [9] G. Gompper, D. A. Fedosov, Modeling microcirculatory blood flow: current state and future perspectives, *Wiley Interdisciplinary Reviews: Systems Biology and Medicine* (2015) n/a–n/a.
- [10] G. Danker, C. Misbah, Rheology of a Dilute Suspension of Vesicles, *Physical Review Letters* 98 (2007).
- [11] T. Krüger, M. Gross, D. Raabe, F. Varnik, Crossover from tumbling to tank-treading-like motion in dense simulated suspensions of red blood cells, *Soft Matter* 9 (2013) 9008–9015.
- [12] D. Cordasco, P. Bagchi, Orbital drift of capsules and red blood cells in shear flow, *Physics of Fluids* 25 (2013) 091902.
- [13] A. Guckenberger, A. Kihm, T. John, C. Wagner, S. Gekle, Numerical-experimental observation of shape bistability of red blood cells flowing in a microchannel, *Soft Matter* (2018).
- [14] P. Olla, The behavior of closed inextensible membranes in linear and quadratic shear flows, *Physica A: Statistical Mechanics and its Applications* 278 (2000) 87–106.
- [15] J. Zhang, Effect of Suspending Viscosity on Red Blood Cell Dynamics and Blood Flows in Microvessels, *Microcirculation* 18 (2011) 562–573.
- [16] G. Ghigliotti, A. Rahimian, G. Biros, C. Misbah, Vesicle Migration and Spatial Organization Driven by Flow Line Curvature, *Physical Review Letters* 106 (2011).
- [17] B. Kaoui, J. Harting, C. Misbah, Two-dimensional vesicle dynamics under shear flow: Effect of confinement, *Physical Review E* 83 (2011) 066319.
- [18] O. Aouane, A. Farutin, M. Thiébaud, A. Benyoussef, C. Wagner, C. Misbah, Hydrodynamic pairing of soft particles in a confined flow, *Physical Review Fluids* 2 (2017).
- [19] M. Toner, D. Irimia, Blood-on-a-Chip, *Annual Review of Biomedical Engineering* 7 (2005) 77–103.
- [20] G. Tomauolo, Biomechanical properties of red blood cells in health and disease towards microfluidics, *Biomicrofluidics* 8 (2014) 051501.
- [21] B. Sebastian, P. S. Dittrich, Microfluidics to Mimic Blood Flow in Health and Disease, *Annual Review of Fluid Mechanics* 50 (2018) 483–504.
- [22] R. Lima, T. Ishikawa, Y. Imai, M. Takeda, S. Wada, T. Yamaguchi, Radial dispersion of red blood cells in blood flowing through glass capillaries: The role of hematocrit and geometry, *Journal of Biomechanics* 41 (2008) 2188–2196.
- [23] T. Yaginuma, M. S. N. Oliveira, R. Lima, T. Ishikawa, T. Yamaguchi, Human red blood cell behavior under homogeneous extensional flow in a hyperbolic-shaped microchannel, *Biomicrofluidics* 7 (2013) 054110.
- [24] S. Roman, A. Merlo, P. Duru, F. Risso, S. Lorthois, Going beyond 20 μm -sized channels for studying red blood cell phase separation in microfluidic bifurcations, *Biomicrofluidics* 10 (2016) 034103.
- [25] S. Yang, A. Ündar, J. D. Zahn, A microfluidic device for continuous, real time blood plasma separation, *Lab on a Chip* 6 (2006) 871–880.

- [26] V. Kantsler, E. Segre, V. Steinberg, Dynamics of interacting vesicles and rheology of vesicle suspension in shear flow, *EPL (Europhysics Letters)* 82 (2008) 58005.
- [27] X. Grandchamp, G. Couplier, A. Srivastav, C. Minetti, T. Podgorski, Lift and Down-Gradient Shear-Induced Diffusion in Red Blood Cell Suspensions, *Physical Review Letters* 110 (2013).
- [28] L. Lanotte, J. Mauer, S. Mendez, D. A. Fedosov, J.-M. Fromental, V. Claveria, F. Nicoud, G. Gompper, M. Abkarian, Red cells' dynamic morphologies govern blood shear thinning under microcirculatory flow conditions, *Proceedings of the National Academy of Sciences* (2016) 201608074.
- [29] C.-H. Chuang, K. Kikuchi, H. Ueno, K. Numayama-Tsuruta, T. Yamaguchi, T. Ishikawa, Collective spreading of red blood cells flowing in a microchannel, *Journal of Biomechanics* 69 (2018) 64–69.
- [30] J. M. Sherwood, D. Holmes, E. Kaliviotis, S. Balabani, Spatial Distributions of Red Blood Cells Significantly Alter Local Haemodynamics, *PLOS ONE* 9 (2014) e100473.
- [31] Z. Shen, G. Couplier, B. Kaoui, B. Polack, J. Harting, C. Misbah, T. Podgorski, Inversion of hematocrit partition at microfluidic bifurcations, *Microvascular Research* 105 (2016) 40–46.
- [32] T. Krüger, *Computer Simulation Study of Collective Phenomena in Dense Suspensions of Red Blood Cells under Shear*, Vieweg+Teubner Verlag, 2012.
- [33] Y. H. Qian, D. D'Humières, P. Lallemand, Lattice BGK Models for Navier-Stokes Equation, *EPL (Europhysics Letters)* 17 (1992) 479.
- [34] P. L. Bhatnagar, E. P. Gross, M. Krook, A Model for Collision Processes in Gases. I. Small Amplitude Processes in Charged and Neutral One-Component Systems, *Physical Review* 94 (1954) 511–525.
- [35] Z. Guo, C. Zheng, B. Shi, Discrete lattice effects on the forcing term in the lattice Boltzmann method, *Physical Review E* 65 (2002) 046308.
- [36] C. S. Peskin, The immersed boundary method, *Acta Numerica* 11 (2002) 479–517.
- [37] M. O. Bernabeu, M. L. Jones, J. H. Nielsen, T. Krüger, R. W. Nash, D. Groen, S. Schmieschek, J. Hetherington, H. Gerhardt, C. A. Franco, P. V. Coveney, Computer simulations reveal complex distribution of haemodynamic forces in a mouse retina model of angiogenesis, *Journal of The Royal Society Interface* 11 (2014) 20140543.
- [38] T. Krüger, F. Varnik, D. Raabe, Efficient and accurate simulations of deformable particles immersed in a fluid using a combined immersed boundary lattice Boltzmann finite element method, *Computers & Mathematics with Applications* 61 (2011) 3485–3505.
- [39] G. R. Cokelet, H. L. Goldsmith, Decreased hydrodynamic resistance in the two-phase flow of blood through small vertical tubes at low flow rates, *Circulation Research* 68 (1991) 1–17.
- [40] D. A. Fedosov, B. Caswell, A. S. Popel, G. E. Karniadakis, Blood Flow and Cell-Free Layer in Microvessels, *Microcirculation* 17 (2010) 615–628.
- [41] S. P. Suter, R. Skalak, The History of Poiseuille's Law, *Annual Review of Fluid Mechanics* 25 (1993) 1–20.
- [42] H. L. Goldsmith, S. G. Mason, Axial Migration of Particles in Poiseuille Flow, *Nature* 190 (1961) 1095–1096.
- [43] B. Lorz, R. Simson, J. Nardi, E. Sackmann, Weakly adhering vesicles in shear flow: Tanktreading and anomalous lift force, *EPL (Europhysics Letters)* 51 (2000) 468.
- [44] M. Abkarian, C. Lartigue, A. Viallat, Tank Treading and Unbinding of Deformable Vesicles in Shear Flow: Determination of the Lift Force, *Physical Review Letters* 88 (2002).
- [45] N. Callens, C. Minetti, G. Couplier, M.-A. Mader, F. Dubois, C. Misbah, T. Podgorski, Hydrodynamic lift of vesicles under shear flow in microgravity, *EPL* 83 (2008) 24002.
- [46] G. Couplier, B. Kaoui, T. Podgorski, C. Misbah, Noninertial lateral migration of vesicles in bounded Poiseuille flow, *Physics of Fluids* 20 (2008) 111702.
- [47] I. Cantat, C. Misbah, Lift Force and Dynamical Unbinding of Adhering Vesicles under Shear Flow, *Physical Review Letters* 83 (1999) 880–883.
- [48] S. Sukumaran, U. Seifert, Influence of shear flow on vesicles near a wall: A numerical study, *Physical Review E* 64 (2001) 011916.
- [49] T. W. Secomb, B. Styp-Rekowska, A. R. Pries, Two-Dimensional Simulation of Red Blood Cell Deformation and Lateral Migration in Microvessels, *Annals of Biomedical Engineering* 35 (2007) 755–765.
- [50] B. Kaoui, G. H. Ristow, I. Cantat, C. Misbah, W. Zimmermann, Lateral migration of a two-dimensional vesicle in unbounded Poiseuille flow, *Physical Review E* 77 (2008) 021903.
- [51] S. K. Dodd, P. Bagchi, Lateral migration of a capsule in a plane Poiseuille flow in a channel, *International Journal of Multiphase Flow* 34 (2008) 966–986.
- [52] S. Meßlinger, B. Schmidt, H. Noguchi, G. Gompper, Dynamical regimes and hydrodynamic lift of viscous vesicles under shear, *Physical Review E* 80 (2009).
- [53] L. Shi, T.-W. Pan, R. Glowinski, Lateral migration and equilibrium shape and position of a single red blood cell in bounded Poiseuille flows, *Physical Review E* 86 (2012).
- [54] D. S. Hariprasad, T. W. Secomb, Prediction of noninertial focusing of red blood cells in Poiseuille flow, *Physical Review E* 92 (2015).
- [55] A. Farutin, C. Misbah, Analytical and Numerical Study of Three Main Migration Laws for Vesicles Under Flow,

- Physical Review Letters 110 (2013) 108104.
- [56] H. Bruus, *Theoretical Microfluidics*, Oxford Master Series in Physics, OUP Oxford, 2008.
 - [57] P. Olla, The lift on a tank-treading ellipsoidal cell in a bounded shear flow, *Journal de Physique II* 7 (1997) 1533–1540. ArXiv: [chao-dyn/9610017](https://arxiv.org/abs/chao-dyn/9610017).
 - [58] A. R. Pries, K. Ley, M. Claassen, P. Gaehtgens, Red cell distribution at microvascular bifurcations, *Microvascular Research* 38 (1989) 81–101.
 - [59] D. Katanov, G. Gompper, D. A. Fedosov, Microvascular blood flow resistance: Role of red blood cell migration and dispersion, *Microvascular Research* 99 (2015) 57–66.
 - [60] S. S. Ye, M. Ju, S. Kim, Recovery of cell-free layer and wall shear stress profile symmetry downstream of an arteriolar bifurcation, *Microvascular Research* 106 (2016) 14–23.
 - [61] Y. C. Ng, B. Namgung, S. L. Tien, H. L. Leo, S. Kim, Symmetry recovery of cell-free layer after bifurcations of small arterioles in reduced flow conditions: effect of RBC aggregation, *American Journal of Physiology - Heart and Circulatory Physiology* 311 (2016) H487–H497.
 - [62] R. Fåhræus, The Suspension Stability of the Blood, *Physiological Reviews* 9 (1929) 241–274.
 - [63] K. H. Albrecht, P. Gaehtgens, A. Pries, M. Heuser, The Fahraeus effect in narrow capillaries (i.d. 3.3 to 11.0 μm), *Microvascular Research* 18 (1979) 33–47.
 - [64] P. Olla, Simplified Model for Red Cell Dynamics in Small Blood Vessels, *Physical Review Letters* 82 (1999) 453–456.
 - [65] U. Seifert, Hydrodynamic Lift on Bound Vesicles, *Physical Review Letters* 83 (1999) 876–879.
 - [66] G. Danker, P. M. Vlahovska, C. Misbah, Vesicles in Poiseuille Flow, *Physical Review Letters* 102 (2009) 148102.
 - [67] S. Nix, Y. Imai, T. Ishikawa, Lateral migration of a capsule in a parabolic flow, *Journal of Biomechanics* 49 (2016) 2249–2254.
 - [68] S. Losserand, G. Coupier, T. Podgorski, Migration velocity of red blood cells in microchannels, *Microvascular Research* (2019).
 - [69] S. Kim, P. K. Ong, O. Yalcin, M. Intaglietta, P. C. Johnson, The cell-free layer in microvascular blood flow, *Biorheology* 46 (2009) 181–189.
 - [70] S. Tripathi, Y. V. B. V. Kumar, A. Prabhakar, S. S. Joshi, A. Agrawal, Passive blood plasma separation at the microscale: a review of design principles and microdevices, *Journal of Micromechanics and Microengineering* 25 (2015) 083001.
 - [71] S. Kim, R. L. Kong, A. S. Popel, M. Intaglietta, P. C. Johnson, Temporal and spatial variations of cell-free layer width in arterioles, *American Journal of Physiology - Heart and Circulatory Physiology* 293 (2007) H1526–H1535.
 - [72] P. K. Ong, S. Jain, S. Kim, Spatio-temporal variations in cell-free layer formation near bifurcations of small arterioles, *Microvascular Research* 83 (2012) 118–125.
 - [73] O. Oulaid, J. Zhang, Cell-free layer development process in the entrance region of microvessels, *Biomechanics and Modeling in Mechanobiology* 14 (2014) 783–794.
 - [74] P. Balogh, P. Bagchi, The cell-free layer in simulated microvascular networks, *Journal of Fluid Mechanics* 864 (2019) 768–806.
 - [75] Q. M. Qi, E. S. G. Shaqfeh, Theory to predict particle migration and margination in the pressure-driven channel flow of blood, *Physical Review Fluids* 2 (2017).
 - [76] R. G. Henríquez Rivera, X. Zhang, M. D. Graham, Mechanistic theory of margination and flow-induced segregation in confined multicomponent suspensions: Simple shear and Poiseuille flows, *Physical Review Fluids* 1 (2016).
 - [77] G. Segré, A. Silberberg, Radial Particle Displacements in Poiseuille Flow of Suspensions, *Nature* 189 (1961) 209–210.
 - [78] J.-S. Park, S.-H. Song, H.-I. Jung, Continuous focusing of microparticles using inertial lift force and vorticity via multi-orifice microfluidic channels, *Lab on a Chip* 9 (2009) 939–948.
 - [79] M. Bouzidi, M. Firdaouss, P. Lallemand, Momentum transfer of a Boltzmann-lattice fluid with boundaries, *Physics of Fluids* 13 (2001) 3452–3459.